A limit analysis approach based on Cosserat continuum for the evaluation of the in-plane strength of discrete media: application to masonry

Michele Godio[a], Ioannis Stefanou[a,*], Karam Sab[a], Jean Sulem[a], Seddik Sakji[b]

[a] *Laboratoire Navier, UMR 8205, École des Ponts, IFSTTAR, CNRS, UPE, Champs-sur-Marne, France*
[b] *Université Paris-Est, Centre Scientifique et Technique du Bâtiment (CSTB), 84 avenue Jean Jaurès, Champs-sur-Marne, 77447 Marne-la-Vallée cedex 2, France*

Abstract

In the frame of Cosserat continuum theory, an upscaling procedure for the assessment of the in-plane strength domain of discrete media is developed. The procedure is the extension to the Cosserat continuum of a procedure initially formulated for the Cauchy continuum, based on the kinematic approach of limit analysis and the classical homogenisation theory. The extension to the Cosserat continuum is made in order to take into account the effect of particles' rotation on the strength of the discrete medium. The procedure is illustrated with regard to periodic assemblies of blocks in contact and is then generalised to the whole class of discrete periodic media with particles of the same type. The case of masonry is considered as an application. Strength criteria of columns and walls are formulated in terms of non-symmetric stresses and in-plane couples. The procedure allows to show how the in-plane strength of the medium is reduced as a result of particles' rotation.

Keywords:
Masonry, Cosserat continuum, Limit analysis, Homogenisation, Upscaling of discrete media

1. Introduction

In the last three decades, a renewed interest towards the Cosserat (or micropolar) continuum has driven researchers to the development of specific models for discrete media such as masonry. Since the original works of Besdo (1985); Mühlhaus (1989); Masiani et al. (1995); Dai et al. (1996); Mühlhaus et al. (1997); Sulem and Mühlhaus (1997) up to the more recent of Stefanou et al. (2008); Addessi et al. (2010); Addessi and Sacco (2012), the resort to the Cosserat continuum has seemed motivated by the advantages enclosed in its enhanced kinematics and the non-symmetry of the stress tensor. Indeed, when used for the formulation of continuum equivalent models for discrete media, Cosserat continuum allows to efficiently take into account high deformation gradients (Trovalusci and Masiani, 2005), relative particles' rotation (Pau and Trovalusci, 2012) and scale effects (Salerno and de Felice, 2009; Godio et al., 2015). Moreover, Cosserat continuum enables the investigation of the phenomenon of wave dispersion, which governs the dynamic response of discrete periodic media when the wavelength is comparable to the size of the microstructure (internal length). Those aspects makes Cosserat-continuum-based models particularly well suited for the description of the mechanical behaviour of masonry structures and preferable, in this sense, with respect to models based on the Cauchy (Salerno and de Felice, 2009) or the second gradient continuum (Trovalusci and Pau, 2014).

The aforementioned features of the Cosserat continuum are strictly related to rotations. Contrary to the Cauchy continuum, rotations in micropolar continua are inherent to the medium, i.e. attached to the

*Corresponding author
Email addresses: michele.godio@enpc.fr (Michele Godio), ioannis.stefanou@enpc.fr (Ioannis Stefanou), karam.sab@enpc.fr (Karam Sab), jean.sulem@enpc.fr (Jean Sulem), seddik.sakji@cstb.fr (Seddik Sakji)

material particle (Germain, 1973; Vardoulakis and Sulem, 1995). Several works have shown how, aiming at representing masonry as an equivalent Cosserat continuum, these rotations are actually representative of blocks' rotations. In particular, they enable a continuum description of the medium which is capable to capture not only the relative rotations occurring between the blocks, but also the relative rotations of the blocks with respect to the local rotation of masonry considered as a whole (Pau and Trovalusci, 2012). The role of rotations is even more apparent in the dynamic regime. Whether regarding the in-plane (Mühlhaus et al., 1997; Sulem and Mühlhaus, 1997) or the out-of-plane behaviour (Stefanou et al., 2008), the mechanical response of masonry is governed by translational and rotational waves. Only their superposition gives the complete structural response. Therefore, blocks' rotations can have a significant participation in the inertial response of masonry, for instance when this latter is subjected to in-plane seismic excitations (Godio et al., 2015).

Nevertheless, the influence of blocks' rotations on the performance of masonry can be far more important than this proportion indicates. Indeed, the rotation of the blocks promotes the relative displacements across the joints, which are the main responsible for energy dissipation in masonry. This may lead to the premature development of macroscopic failure mechanisms. Even though this aspect is visible from the majority of the experimental tests carried out on masonry structures (see the recent tests by Petry and Beyer (2014a)), it has been seldom explored in the corresponding literature, see for instance Besdo (1985); Sulem and Mühlhaus (1997); Trovalusci and Masiani (2003, 2005); Addessi and Sacco (2012).

The purpose of the present paper is to determine the in-plane strength of discrete media starting from the knowledge of their constituents only. This is made by distinguishing and bridging two observations scales or levels. The application to masonry illustrates the advantages of the formulation. At the microscopic scale, masonry is regarded as a discrete medium, that is an assemblage of rigid blocks. The deformation though is considered to be concentrated at the interfaces of the blocks (soft-contacts). The assumption of rigid blocks with deformable interfaces is common in the literature for discrete granular media and blocky structures and removes the indeterminacy of the system (e.g. Besdo (1985); Masiani et al. (1995); Cecchi and Sab (2004); Cecchi et al. (2007)). Herein, a rigid-plastic formulation is followed for the interfaces. In particular the blocks interact with each other through Coulomb interfaces, representing the masonry joints. Failure corresponds to the use of the strength capacities of the joints only, and not of the blocks, which are considered infinitely resistant (cf. Stefanou et al. (2015)). In particular, whether engendered by the relative blocks' translation or rotation, joints' failure is accounted for by a unique Coulomb slip criterion. At the macroscopic scale, masonry is described by a 2D Cosserat continuum. The determination of its strength domain is made by means of a rigorous homogenisation (to be intended herein as upscaling) procedure specifically developed for Cosserat continua and based on the use of the kinematic approach of limit analysis.

The present work can be seen as an extension to the Cosserat continuum of the homogenisation procedure proposed by de Buhan and de Felice (1997) and further developed by Sab (2003) and Sab et al. (2007). That procedure was based on the Cauchy continuum and made use of the asymptotic homogenisation of periodic media. In that context, the rotations of the blocks of masonry were controlled by the macroscopic displacement field. For that reason, additional contraints were to be added to the formulation. In the upscaling procedure followed here, rotations are left free and consist in additional degrees of freedom whose average on the unit cell can be straightforwardly related to the macroscopic Cosserat rotation. The proposed upscaling is therefore apt for describing in a continuous manner the mechanical behaviour of mono-atomic discrete media with periodic inner micro-structure (Florence and Sab, 2006; Stefanou et al., 2008; Stefanou and Sulem, 2012), to which also masonry belongs. The formulation is based upon the *homogeneous equivalent continuum* concept (Charalambakis, 2010), in the sense that the derived Cosserat continuum shares a) the same energy (dissipation) and b) the same kinematics with the discrete medium. We do not follow the classical asymptotic homogenisation ansatz that leads to a Cauchy continuum as the ratio of the size of the unit cell over the overall structure tends to zero. By this pass to the limit, asymptotic homogenisation tends to erase any internal length related to the material micro-structure, that higher order continuum theories such as the Cosserat one are, on the contrary, able to capture (Forest and Sab, 1998; Pradel and Sab, 1998; Forest et al., 2001). For this reason, the proposed procedure remains valuable when the size of the micro-structure is important compared to the overall size of the structure, that is when scale separation is no more applicable. As such, it will depend on the choice of the elementary cell. On the contrary, the

obtained Cosserat continuum converges asymptotically to the Cauchy continuum given by the asymptotic homogenisation, when the relative size of the micro-structure tends to vanish (Pradel and Sab, 1998).

At present, very few works have shown the use of the Cosserat medium in inelasticity. One can cite the work by Rezakhani and Cusatis (2016) and some older works in plasticity concerning the macroscopic behavior of reinforced soils and rock assemblies (de Buhan et al., 1998, 2002). It is worth noticing that the resort to the micropolar theory for the assessment of masonry in-plane strength was indicated by de Buhan and de Felice (1997) as crucial for capturing the scale effect observed in the failure mechanisms resulted from full-scale tests. Therefore, although the yield criteria computed for the Cosserat continuum may always give upper bounds of the researched strength domain, they are supposed to be better estimates of the *actual* strength capacity of the material as compared to those computed for the Cauchy continuum. The reason may be found, once again, in the enhanced kinematics of the adopted continuum. On one hand, they provide an improved estimation of the power dissipated by the discrete medium. On the other hand, they allow a finer reproduction of the deformation modes and failure mechanisms of the medium (upper bound theorem of limit analysis).

The present work differs from the aforementioned works (Rezakhani and Cusatis, 2016; de Buhan et al., 1998, 2002), as it aims at providing a rigorous upscaling scheme based on the kinematic approach of limit analysis and provides (semi-)analytically the ultimate strength of discrete particle assemblies in the frame of Cosserat continuum. Moreover, various aspects related to a) the connection and the physical meaning of the generalised stress and deformation measures of the upscaled Cosserat continuum with the kinematics of the discrete microstructure and b) the effect of the size of the chosen elementary cell are discussed in detail thorough illustrative examples that are treated analytically. In particular, the paper has the following structure. A brief summary of the equations governing the micropolar medium is first given in Section 2. The contact model adopted for the discrete media and on which the upscaling procedure is illustrated, is presented next in Section 3. Cosserat macroscopic variables are then computed as average values of the discrete ones. The upscaling procedure is presented for the contact model first and it is then generalised for generic discrete periodic media (Section 4). Further in Section 5 and Section 6, two applications are described. In Section 5 homogenisation is carried on the illustrative example of a simple masonry column. In Section 6, homogenisation is performed on a masonry wall, with building blocks arranged following a generic periodic pattern and interface joints showing different dissipative properties depending on their orientation. Comparisons with existing works are made in Section 7. They show the advantages of the presented upscaling procedure, by highlighting the role of relative blocks' rotations in the evaluation of the in-plane strength of masonry and, more generally, of discrete media.

It is worth emphasizing that the term homogenisation used in several places in this paper refers to the proposed upscaling procedure and not to the asymptotic homogenisation. Indicial notation is adopted throughout the paper, with Greek indices $\alpha, \beta, \gamma, \ldots$ ranging between 1 and 2. Einstein summation applies for repeated indices. Lower case letters denote variables referring to the discrete medium, while upper case letters refer to the macroscopic variables of the Cosserat continuum. Partial differentiation with respect to orthogonal coordinates is denoted with $[\ ]_{\alpha,\beta}$, while $\partial_{X_\beta}[\ ]_\alpha$ designates tensor derivative. Time derivative $[\ ]_{\alpha,t}$ is indicated with $[\dot{\ }]_\alpha$.

2. The Cosserat continuum: 2D formulation and strength

Cosserat (or micropolar) continuum is a special case of a micromorphic continuum of first order (Eringen, 1999; Germain, 1973; Godio et al., 2015). In this case, the material particle is associated with a rigid oriented triad (Figure 1) which, when the medium undergoes deformation, experiences displacement velocities V_α (or translations), and angular displacement velocities Ω^c (or rotations). The rate of the linear deformation measures of the medium is given by two second order tensors (Schaefer, 1967; Germain, 1973; Vardoulakis and Sulem, 1995). The first tensor is denoted by $\Gamma_{\alpha\beta}$ and accounts for the relative deformation occurring between the rate of the displacement gradient $D_{\alpha\beta}$ and the Cosserat (or particle) rotation Ω^c:

$$\Gamma_{\alpha\beta} = D_{\alpha\beta} + e_{\alpha\beta}\Omega^c, \tag{1}$$

with:

$$D_{\alpha\beta} = V_{\alpha,\beta}, \tag{2}$$

and $e_{\alpha\beta}$ the 2D Levi-Civita's symbol. $\Gamma_{\alpha\beta}$ is a non-symmetric tensor and is decomposed into its symmetric $\Gamma_{(\alpha\beta)}$ and skew-symmetric $\Gamma_{[\alpha\beta]}$ parts as follows:

$$\Gamma_{\alpha\beta} = \Gamma_{(\alpha\beta)} + \Gamma_{[\alpha\beta]}, \tag{3}$$

reading:

$$\Gamma_{(\alpha\beta)} = D_{(\alpha\beta)}, \quad \Gamma_{[\alpha\beta]} = D_{[\alpha\beta]} + e_{\alpha\beta}\Omega^c. \tag{4}$$

The second tensor accounts for the rate of the rotation gradient (or curvature) of the medium. In the two-dimensional case, where only the in-plane rotations Ω^c are considered, it reduces to:

$$K_\beta = \Omega^c_{,\beta}. \tag{5}$$

In the Cauchy continuum the rigid triad is non-oriented (Figure 1), and the kinematics of the material particle, considered as a point, is described by the translations V_α only. The deformation measures of the medium reduce then to the symmetric tensor $D_{(\alpha\beta)}$ (Eq.(4)-1), contrary to the Cosserat continuum, where the skew-symmetric part of the relative deformations $D_{[\alpha\beta]}$ is non-null and related to the particle rotations (Eq.(4)-2). The microstretch continuum is a first generalization of the Cosserat continuum (Eringen, 1999). In that case, in addition to the translations and rotations, the material particle experiences also volume changes, that is micro-contractions and expansions (Figure 1). In the micromorphic continuum the material particle is considered as fully-deformable, carrying an oriented triad and undergoing any kind of micro-deformation.

the particle as a material point	*the particle as a rigid body*	*the particle as a volume-deformable body*	*the particle as a fully-deformable body*
Simple (Cauchy)	Micropolar (Cosserat)	Microstrecth	Micromorphic

Figure 1: Classes of continuum media according to Eringen (1999).

The static variables associated to $\Gamma_{\alpha\beta}$ and K_β are respectively $T_{\alpha\beta}$ and M_β. They denote respectively the in-plane components of the non-symmetric stress tensor and of the couple stress tensor. The convention used for those tensors follows Vardoulakis and Sulem (1995): the first index gives the direction of the component and the second index the oriented face where this component is applied (see Figure 2-left). With this notation, the internal power density of the Cosserat continuum reads:

$$P^c = T_{\alpha\beta}\Gamma_{\alpha\beta} + M_\beta K_\beta. \tag{6}$$

In this paper we focus on the formulation of the strength domain of discrete media, considered as an equivalent 2D Cosserat continuum at the macroscopic scale. The strength domain in a Cosserat material is defined as the convex region of the generalised stress space $(T_{\alpha\beta}, M_\beta)$ which is bounded by multiple N_F and intersecting plastic surfaces $F_j = F_j\,(T_{\alpha\beta}, M_\beta)$, representing the yield criteria (Lippmann, 1969; Steinmann, 1994):

$$G^c = \{(T_{\alpha\beta}, M_\beta)\,|F_j\,(T_{\alpha\beta}, M_\beta) \leq 0, \forall j = 1, \ldots, N_F\}. \tag{7}$$

Another definition of the strength domain alternative to the *direct* (Salençon, 2013) definition (7) follows from the expression of the maximum dissipation principle. This principle states that, upon deformation,

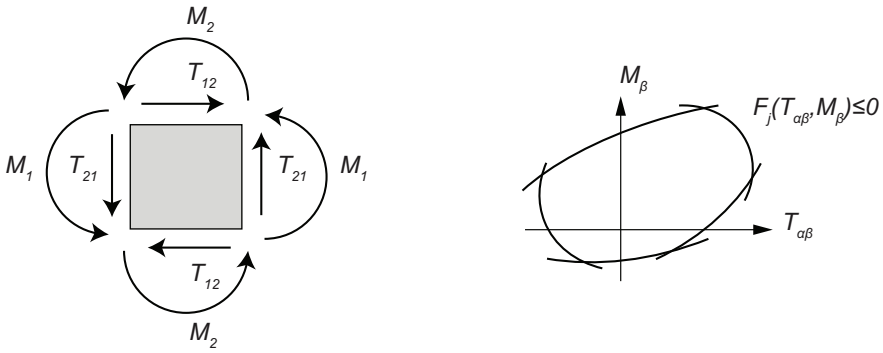

Figure 2: Stresses and couple stresses of a 2D Cosserat continuum (left). Its strength domain is formulated as the convex region of the generalised space $(T_{\alpha\beta}, M_\beta)$ enclosed by multiple plastic surfaces (right).

the plastic dissipation, herein denoted with $\Pi^c = \Pi^c(\Gamma_{\alpha\beta}, K_\beta)$, attains its maximum for the actual stress tensor. In a Cosserat medium and in the case of perfect plasticity (no hardening), the principle reads:

$$\Pi^c = \sup_{(T_{\alpha\beta}, M_\beta) \in G^c} \{T_{\alpha\beta}\Gamma_{\alpha\beta} + M_\beta K_\beta\}\,. \tag{8}$$

One recognizes in Π^c the support function of G^c. Eq.(8) then leads to the second, referred to as *kinematic* (Salençon, 2013), definition of the strength domain, useful for the sequel, which writes:

$$G^c = \{(T_{\alpha\beta}, M_\beta)\,|T_{\alpha\beta}\Gamma_{\alpha\beta} + M_\beta K_\beta \leq \Pi^c, \forall(\Gamma_{\alpha\beta}, K_\beta)\}. \tag{9}$$

3. The discrete medium: discrete variables and contact model

The material considered at the microscopic scale has a inner structure consisting of a discrete collection of rigid interacting bodies (or blocks) that translate and rotate in space. The blocks are arranged following a periodic lattice and form elementary cells in the form of geometrical figures, like rectangles, hexagons, etc. All blocks share the same shape and size. Their position within the lattice is marked in a global reference system (O, Y_1, Y_2) by two periodicity vectors $\boldsymbol{\alpha^i}$ $(i = 1, 2)$ and reads:

$$\boldsymbol{Y^{GJ}} = \boldsymbol{Y^{G0}} + \mathrm{n}\boldsymbol{\alpha^1} + \mathrm{m}\boldsymbol{\alpha^2} \tag{10}$$

where GJ represents the centre of mass G of the block B^J, with $J = 1, \ldots, N$ and $(\mathrm{n}, \mathrm{m}) \in \mathbb{Z}^2$. This configuration is often referred to as *mono-atomic* lattice (Kittel, 1996).

We focus on D, the elementary cell repeated in the lattice. It is worth emphasizing that the choice of the elementary cell is not unique and that the resulting continuum depends on this choice. This is owed to the fact that the upscaled continuum possesses internal lengths, contrary to the classical, Boltzmann continuum (Vardoulakis, 2009), that is internal-length-free. The influence of the choice and size of the elementary cell is discussed further in Section 5.4. One direct choice of D is to consider as lattice points of the inner micro-structure, the centres of mass of the blocks GJ, and as basis, the periodicity vectors $\boldsymbol{\alpha^i}$ (Figure 3). In this way, the lattice points are kept only at the corners of the cell and the periodicity vectors coincide with the *primitive basis* of the lattice (Kittel, 1996). Of course any other points could be chosen as reference points, but this choice simplifies the algebraic calculations and the average Cosserat expressions of the resulting continuum (e.g. Section 6.2). Moreover, this cell represents for the discrete medium the structural unit with the smallest surface required for the description of its behaviour (Kittel, 1996):

$$|D| = |\boldsymbol{\alpha^1} \times \boldsymbol{\alpha^2}|. \tag{11}$$

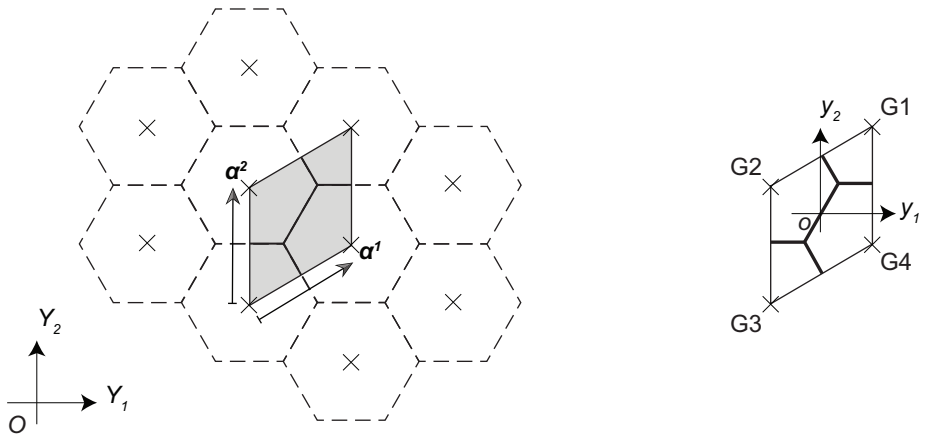

Figure 3: A periodic collection of discrete blocks and the corresponding elementary cell. The elementary cell retained (right) is the parallelogram produced by the periodicity vectors.

A local reference system (o, y_1, y_2) is attached to D and N_D denotes the number of blocks J that compose the cell (in this case $J = 1, \ldots, N_D$). For rigid blocks, the kinematics of the whole cell is described by piece-wise linear distributions the translational and angular velocity fields, v_α and ω, of the form:

$$\begin{aligned} v_\alpha^J(\boldsymbol{y}) &= v_\alpha^{\mathrm{G}J} - e_{\alpha\beta}\omega^{\mathrm{G}J}\left(y_\beta - y_\beta^{\mathrm{G}J}\right) \\ \omega^J(\boldsymbol{y}) &= \omega^{\mathrm{G}J}, \forall \boldsymbol{y} \in B^J, \end{aligned} \tag{12}$$

where $v_\alpha^{\mathrm{G}J}$ and $\omega^{\mathrm{G}J}$ are respectively the translational and rotational velocities of the centre of mass G of the block B^J. These kinematics represent the degrees of freedom of the discrete cell (Figure 4-left):

$$\begin{aligned} v_\alpha^{\mathrm{G}J} &= v_\alpha\left(\boldsymbol{y}^{\mathrm{G}J}\right) \\ \omega^{\mathrm{G}J} &= \omega\left(\boldsymbol{y}^{\mathrm{G}J}\right). \end{aligned}$$

Contact kinematics Contact statics

Figure 4: Kinematics and statics of the contact model adopted for the discrete medium.

Blocks may have arbitrary shape and their external surface may be in contact only with the surface of neighbouring blocks. In particular, the block I interacts with the adjacent block J through contact stresses r_α^{IJ}, at every point of the interface Σ^{IJ} (Figure 4-right). Contact stresses are associated to the displacement velocity jumps (or relative displacements) occurring across the interfaces shared by the blocks:

$$[\![v_\alpha]\!]^{IJ} = v_\alpha^I(\boldsymbol{y}) - v_\alpha^J(\boldsymbol{y}), \forall \boldsymbol{y} \in \Sigma^{IJ}. \tag{13}$$

The internal power density of the cell is then:

$$p^D = \frac{1}{|D|}\left(\sum_{IJ}\int_{\Sigma^{IJ}} r_\alpha^{IJ}[\![v_\alpha]\!]^{IJ}\mathrm{dL}\right), \tag{14}$$

where the sum is made over all the interfaces of the cell.

The relative displacements (13) produce both gaps and slips between the blocks (Figure 5). Those two basic mechanisms are due respectively to the opening and the sliding of the interfaces. They are described by the normal $[\ ]^{\sigma}$ and tangential $[\ ]^{\tau}$ components of the relative displacements:

$$[\![v_\alpha]\!]^{\sigma} = [\![v_\beta]\!]^{IJ} \mathrm{n}_\beta^{IJ} \mathrm{n}_\alpha^{IJ}, \quad [\![v_\alpha]\!]^{\tau} = [\![v_\alpha]\!]^{IJ} - [\![v_\alpha]\!]^{\sigma}. \tag{15}$$

These components are conjugate in energy to respectively the normal and tangential components of the contact stresses, reading:

$$r_\alpha^{\sigma} = r_\beta^{IJ} \mathrm{n}_\beta^{IJ} \mathrm{n}_\alpha^{IJ}, \quad r_\alpha^{\tau} = r_\alpha^{IJ} - r_\alpha^{\sigma}, \tag{16}$$

with n_α^{IJ} the unit vector normal to the interface Σ^{IJ}. No contact moments are considered at each point of the interfaces. This is a reasonable assumption for the applications considered herein. Nevertheless, a transfert of moments is always possible between two adjacent blocks, as the distribution of the stresses is not necessarily constant. Resultant contact moments (or couples) are in fact those generated by first order moments of r_α^{σ} (Bardet and Vardoulakis, 2001). These are associated to the angular displacement velocity jumps:

$$[\![\omega]\!]^{IJ} = \omega^I - \omega^J, \tag{17}$$

which coincide with the rigid-body rotation jumps (relative blocks' rotations):

$$[\![\omega^{\mathrm{G}}]\!]^{IJ} = \omega^{\mathrm{G}I} - \omega^{\mathrm{G}J}. \tag{18}$$

Resultant contact forces, in turn, are generated by r_α^{σ} and r_α^{τ}, and are associated to the rigid-body displacement jumps (relative blocks' translations):

$$[\![v_\alpha^{\mathrm{G}}]\!]^{IJ} = v_\alpha^{\mathrm{G}I} - v_\alpha^{\mathrm{G}J}. \tag{19}$$

It is apparent how the relative rotations and relative translations are both related to interface failure (Figure 5).

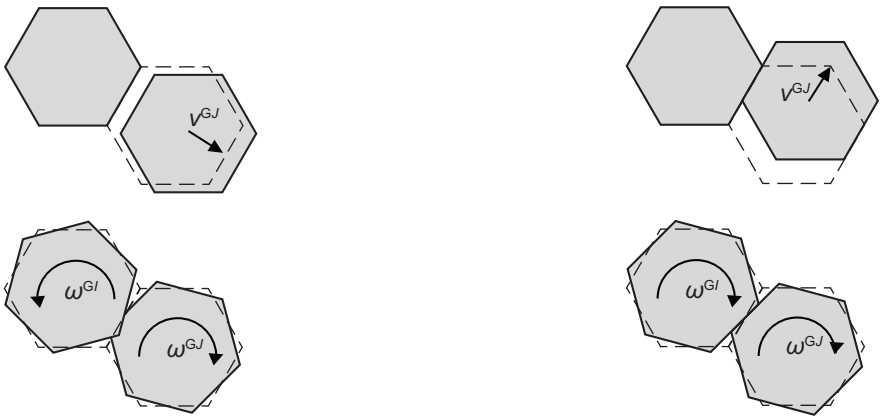

Interface opening Interface sliding

Figure 5: Relative translations $[\![v_\alpha^{\mathrm{G}}]\!]^{IJ}$ and rotations $[\![\omega^{\mathrm{G}}]\!]^{IJ}$ producing opening and sliding of the interface between two blocks. Both depicted mechanisms are related to interface failure.

The strength capacity of each interface is described by g^{IJ}, a convex domain characterised by multiple N_f yield criteria $f_j = f_j\left(r_\alpha^{IJ}\right)$:

$$g^{IJ} = \{\left(r_\alpha^{IJ}\right) | f_j\left(r_\alpha^{IJ}\right) \leq 0, \forall j = 1, .., N_f\}. \tag{20}$$

A kinematic condition for the interface failure is then:

$$r_\alpha^{IJ} \in g^{IJ} \Leftrightarrow r_\alpha^{IJ} [\![v_\alpha]\!]^{IJ} \leq \pi^{IJ}, \forall [\![v_\alpha]\!]^{IJ}, \tag{21}$$

where the support function $\pi^{IJ} = \pi^{IJ}([\![v_\alpha]\!]^{IJ})$ represents the maximum plastic dissipation at the interface. Its definition is as follows (Salençon, 2013):

$$\pi^{IJ} = \underset{r_\alpha^{IJ} \in g^{IJ}}{\text{Sup}} \left\{ r_\alpha^{IJ} [\![v_\alpha]\!]^{IJ} \right\}. \tag{22}$$

Admitting that all interfaces attain failure simultaneously and a failure mechanism is produced within the discrete cell, the amount of plastic dissipation in D is then:

$$\pi^D = \frac{1}{|D|} \left(\sum_{IJ} \int_{\Sigma^{IJ}} \pi^{IJ}([\![v_\alpha]\!]^{IJ}) \mathrm{dL} \right). \tag{23}$$

4. Average Cosserat variables and kinematic approach

The purpose of homogenisation is to replace the discrete medium by a continuum homogeneous medium that has the same shape and shares the same mechanical properties with the discrete ones.

In the present paper, upscaling is carried out in the framework of limit analysis. In this case, one aims at substituting the discrete by a continuum medium that has 1) similar deformation modes and 2) equivalent dissipation properties (Charalambakis, 2010). Here the discrete medium is identified with the continuum at the cell level by means of a kinematic map. Moreover, in such context the principle of maximum plastic dissipation expressed for the Cosserat and the discrete medium plays a fundamental role. This principle has, as main implications (Simo and Hughes, 1998): a) the condition for the plastic potentials of being associative, and b) the convexity of the strength domain in the stress space. The same results hold true when the plasticity theory is formulated in the space of the deformations, for materials with elastic-perfectly plastic behaviour (Naghdi and Trapp, 1975). Under these assumptions the two fundamental theorems of limit analysis are applicable.

4.1. Kinematic map

We focus on the elementary cell D and we define with $KA(V_\alpha, \Omega^c)$ the set of kinematically admissible (or compatible, Eq.(1)) translations and rotations $\left(v_\alpha^{\mathrm{G}J}, \omega^{\mathrm{G}J}\right)$ of the cell as follows:

$$KA(V_\alpha, \Omega^c) = \left\{ \left(v_\alpha^{\mathrm{G}J}, \omega^{\mathrm{G}J}\right) | v_\alpha^{\mathrm{G}J} = D_{\alpha\beta} y_\beta^{\mathrm{G}J} + V_\alpha,\ \omega^{\mathrm{G}J} = K_\beta y_\beta^{\mathrm{G}J} + \Omega^c, \forall J = 1, \ldots, N_D \right\}. \tag{24}$$

From a mechanical point of view, Eq.(24) gives the map between the kinematics of the discrete medium and the deformation measures of the Cosserat continuum. Such map is linear and is defined on the elementary cell of the discrete medium. It is a special case of the map proposed by Pradel and Sab (1998). Here it is adapted for discrete media with mono-atomic pattern, i.e. composed by particles of the same size and shape. The same map can be retrieved from the use of other homogenisation techniques used in the literature. These are based, for instance, on the differential expansion (Pasternak and Mühlhaus, 2005; Stefanou et al., 2008), direct identification (Masiani et al., 1995; Trovalusci and Masiani, 2005), development in Taylor series (Kim, 1983) or polynomial expansions (Bardet and Vardoulakis, 2001) of the velocity and displacement velocity fields of the discrete medium with the continuum ones.

Using the map (24), the displacement and angular displacement velocity fields (12) become:

$$\begin{aligned} v_\alpha^J(\boldsymbol{y}) &= \left(D_{\alpha\beta} + e_{\alpha\beta}\Omega^c\right) y_\beta^{\mathrm{G}J} + V_\alpha - e_{\alpha\beta}\left[K_\gamma y_\gamma^{\mathrm{G}J}\left(y_\beta - y_\beta^{\mathrm{G}J}\right) + \Omega^c y_\beta\right] \\ \omega^J(\boldsymbol{y}) &= K_\beta y_\beta^{\mathrm{G}J} + \Omega^c, \forall \boldsymbol{y} \in B^J. \end{aligned} \tag{25}$$

Eq.(25) constitutes an alternative definition to (24) of kinematically admissible displacement and angular displacement velocity fields obeying Eq.(12). This definition can be used for upscaling, as illustrated next for the presented contact model.

4.2. Average Cosserat variables

The rate of relative deformation $\Gamma_{\alpha\beta}$,and curvature K_β that enter Eq.(25) have a precise physical meaning. They represent the average Cosserat deformation measures of the discrete cell. Their expression follows straightforwardly from the map (24) and depends on the selected cell D. When the cell is constructed as illustrated in Section 3 and the local reference system is attached to the centre of mass of the cell, they write:

$$\Gamma_{\alpha\beta} = \frac{1}{|D|}\left(\sum_{IJ}\int_{\Sigma^{IJ}} [\![v_\alpha]\!]^{IJ} \mathrm{n}_\beta^{IJ}\mathrm{dL}\right) \tag{26}$$

$$K_\beta = \frac{1}{|D|}\left(\sum_{IJ}\int_{\Sigma^{IJ}} [\![\omega]\!]^{IJ} \mathrm{n}_\beta^{IJ}\mathrm{dL}\right), \tag{27}$$

with the relative displacement and rotations given by Eqs.(13) and (17). By definition, $\Gamma_{\alpha\beta}$ gathers the displacement gradient $D_{\alpha\beta}$ and the Cosserat rotation Ω^c. The former identifies the average value of the relative blocks' translations (19), i.e.:

$$D_{\alpha\beta} = \frac{1}{|D|}\left(\sum_{IJ}\int_{\Sigma^{IJ}} [\![v_\alpha^{\mathrm{G}}]\!]^{IJ} \mathrm{n}_\beta^{IJ}\mathrm{dL}\right). \tag{28}$$

The latter, Ω^c, is the average rigid-body cell rotation:

$$\Omega^c = \frac{1}{|D|}\left(\sum_{J=1}^{N_D}\int_{B^J} \omega^J \mathrm{dS}\right). \tag{29}$$

Similarly, V_α is the average rigid-body cell translation:

$$V_\alpha = \frac{1}{|D|}\left(\sum_{J=1}^{N_D}\int_{B^J} v_\alpha^J \mathrm{dS}\right). \tag{30}$$

For the demonstration of Eqs.(26)-(30) the reader is referred to Appendix A. It is worth pointing out that the only average deformation measure for the Cauchy continuum would be (de Buhan and de Felice, 1997):

$$D_{(\alpha\beta)} = \frac{1}{|D|}\left(\sum_{IJ}\frac{1}{2}\int_{\Sigma^{IJ}} \left([\![v_\alpha^{\mathrm{G}}]\!]^{IJ} \mathrm{n}_\beta^{IJ} + [\![v_\beta^{\mathrm{G}}]\!]^{IJ} \mathrm{n}_\alpha^{IJ}\right)\mathrm{dL}\right). \tag{31}$$

By substituting Eq.(25) into the expression of the internal power density of the cell p^D (Eq.(14)), one retrieves:

$$p^D = T_{\alpha\beta}\Gamma_{\alpha\beta} + M_\beta K_\beta, \tag{32}$$

where the non-symmetric stresses:

$$T_{\alpha\beta} = \frac{1}{|D|}\left(\sum_{IJ}\int_{\Sigma^{IJ}} r_\alpha^{IJ} l_\beta^{IJ}\mathrm{dL}\right) \tag{33}$$

and the couple stresses:

$$M_\beta = \frac{1}{|D|}\left(\sum_{IJ}\int_{\Sigma^{IJ}} -e_{\alpha\gamma} r_\alpha^{IJ}\left(y_\gamma l_\beta^{IJ} - y_\gamma^{\mathrm{G}I} y_\beta^{\mathrm{G}I} + y_\gamma^{\mathrm{G}J} y_\beta^{\mathrm{G}J}\right)\mathrm{dL}\right) \tag{34}$$

are found to be the average values of the contact stress distributions exchanged between the blocks of the cell. In the above, l_β^{IJ} is the vector connecting the centre of mass of two adjacent blocks I and J: $l_\beta^{IJ} = y_\beta^{GI} - y_\beta^{GJ}$. The physical meaning of the deformation and stress measures of the Cosserat continuum with respect to those of the presented contact model is clear from the above equations.

4.3. Kinematic approach of limit analysis

The upscaling procedure followed in this paper aims at the extension to the Cosserat continuum of a procedure initially formulated for the Cauchy continua in the framework of the asymptotic homogenisation (Suquet, 1983). That procedure was based on the upper bound theorem of limit analysis and, for this reason, it was called *kinematic approach* within the framework of the yield design theory, see also Salençon (2013). Formulated for the Cosserat continuum, the kinematic approach consists in finding among the established displacement and angular displacement velocity fields (in this case Eq.(25)), the sets of kinematically admissible blocks' translations and rotations $(v_\alpha^{GJ}, \omega^{GJ}) \in KA(V_\alpha, \Omega^c)$ that solves the following problem:

$$\Pi^{c,hom} = \pi^D. \tag{35}$$

The above equation equates the maximum plastic dissipation density produced by the discrete cell π^D (Eq.(23)) with $\Pi^{c,hom}$, representing the maximum plastic dissipation of the homogenised (or *equivalent* (Charalambakis, 2010)) Cosserat continuum (Eq.(8)). Solution to the above problem is found only when the $KA(V_\alpha, \Omega^c)$ kinematics of the discrete medium generate on the cell plastic dissipation of finite value, i.e.:

$$\pi^D \left(v_\alpha^{GJ}, \omega^{GJ}\right) < \infty. \tag{36}$$

This latter condition is essential and use of the upper bound theorem of limit analysis must be made only when Eq.(35) is used in conjunction with it. The kinematic definition of the homogenised strength domain $G^{c,hom}$ follows immediately from the expression of $\Pi^{c,hom}$, this latter being the support function of $G^{c,hom}$ (Eq.(9)):

$$G^{c,hom} = \{(T_{\alpha\beta}, M_\beta) \,|T_{\alpha\beta}\Gamma_{\alpha\beta}^p + M_\beta K_\beta^p \leq \Pi^{c,hom}, \forall(\Gamma_{\alpha\beta}^p, K_\beta^p)\}. \tag{37}$$

The resulting homogenisation procedure is illustrated in Figure 6. Starting from a failure criterion expressed at the interfaces of the discrete medium, it is possible to retrieve the homogenised yield criterion for the macroscopic Cosserat continuum. The resulting strength domain is the region of the generalised stress space $(T_{\alpha\beta}, M_\beta)$ enclosed by these yield criteria. It is worth emphasizing that, as a result of the kinematic approach, the procedure provides upper bound estimates of the actual strength capacity of the discrete medium, exactly as in its original version (Suquet, 1983).

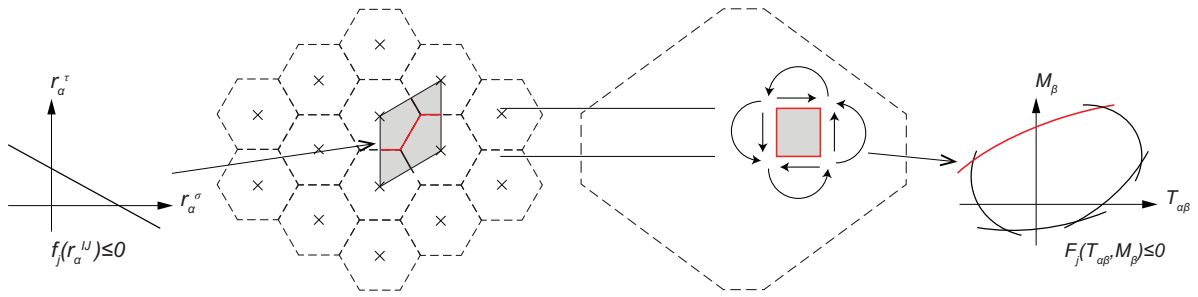

Figure 6: Schematic illustration of the proposed upscaling procedure, based on the Cosserat continuum and carried out in the frame of limit analysis for periodic collections of rigid particles.

4.4. Extension to generic periodic media

The homogenisation procedure has been illustrated according to the contact model presented in Section 3. Such model is representative of a class of media, like soils, fractured rock masses, masonry structures, etc. Nevertheless, the proposed procedure can cover the whole class of discrete periodic media with mono-atomic pattern. An example of application is given in Figure 7, where a grid-work is represented, based on the same mono-atomic lattice used for the contact model (Figure 3). In this case, the lattice points represent the nodes of the grid-work. It is clear that, when these latter are considered rigid, the kinematic description of the whole medium reduces to the degrees of freedom of the nodes, and a micropolar description of the medium can be then attempted (Kumar and McDowell, 2004).

The same considerations apply for generic discrete media, where translations and rotations may always be attached to the distinct interacting particles. Therefore, starting from the kinematics $\left(v_\alpha^{\mathrm{G}J}, \omega^{\mathrm{G}J}\right)$ of a pair of particles I and J, it is possible to define in a general way the following generalised deformation measures (Florence and Sab, 2006):

$$\begin{aligned} d_\alpha^{IJ} &= \left[\!\left[v_\alpha^{\mathrm{G}}\right]\!\right]^{IJ} + e_{\alpha\beta} l_\beta^{IJ} \frac{\omega^{\mathrm{G}I} + \omega^{\mathrm{G}J}}{2} \\ \delta^{IJ} &= \left[\!\left[\omega^{\mathrm{G}}\right]\!\right]^{IJ}. \end{aligned} \tag{38}$$

Without the need of specifying the power-conjugate variables, the power dissipated by the pair of particles is function of the above deformations: $\hat{\pi}^{IJ} = \hat{\pi}^{IJ}(d_\alpha^{IJ}, \delta^{IJ})$. Hence, the amount of plastic dissipation density on the cell writes:

$$\pi^D\left(v_\alpha^{\mathrm{G}J}, \omega^{\mathrm{G}J}\right) = \frac{1}{|D|}\left(\sum_{IJ} \hat{\pi}^{IJ}(d_\alpha^{IJ}, \delta^{IJ})\right). \tag{39}$$

where, in this case, the sum is made over all the particle pairs of the cell, see Eq.(23). in particular, the particle pairs shared by adjacent cells will be accounted by half of their power. Homogenisation is made over the discrete medium as illustrated in the previous sections. Map (24) allows to substitute the Cosserat continuum into the generic discrete medium, reproducing its kinematics and deformation modes (Eqs.(26)-(30)). Eq.(35) then assures that the two media have equivalent plastic dissipation.

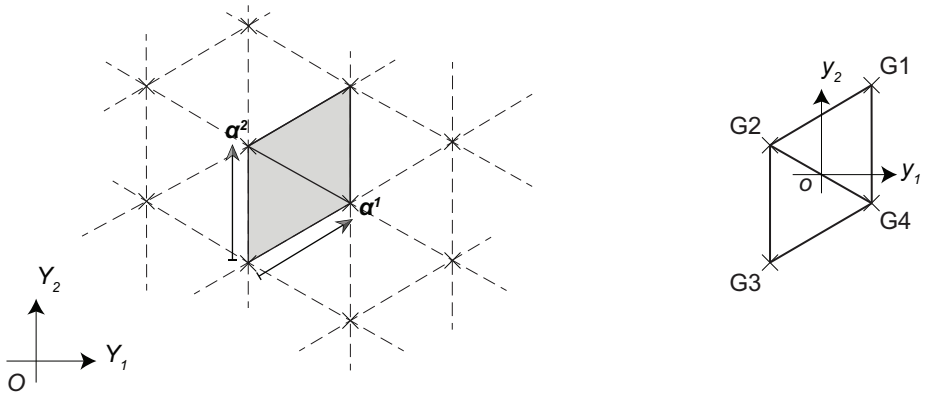

Figure 7: A periodic collection of beams disposed following a mono-atomic lattice (left), and the corresponding elementary cell (right).

5. Application to masonry columns

The method illustrated in Section 4 is herein applied to the case of masonry columns made of distinct blocks of the same size and shape. It is worth remarking that the rate of plastic deformations to which the continuum undergoes is noted generally as a total rate of (irreversible) deformation. Consistently, but not restrictively, we are assuming that blocks' interaction in masonry has a rigid-plastic behaviour.

5.1. Geometry

Masonry columns are quasi periodic assemblages of rectangular blocks stacked in the vertical direction y_2 (Figure 8). The height and the width of each block are denoted respectively with a and b. In such situation, a single vector describes the period of the structure, that is: $\boldsymbol{\alpha^1} = 0\mathbf{e_1} + a\mathbf{e_2}$.

The chosen elementary cell is denoted with B and is referred to a specific local coordinate system (oy1y2) attached to its center. It contains two half blocks, $B1$ and $B2$, and their interface Σ^{12}. Larger elementary cells are investigated in Section 5.4. The position of the centre of mass of each block is:

$$\boldsymbol{y^{G1}} = 0\mathbf{e_1} + \frac{a}{2}\mathbf{e_2}$$
$$\boldsymbol{y^{G2}} = 0\mathbf{e_1} - \frac{a}{2}\mathbf{e_2}.$$

The interface between the blocks Σ^{12} has unit normal vector $\mathbf{n^{12}} = \mathbf{e_2}$.

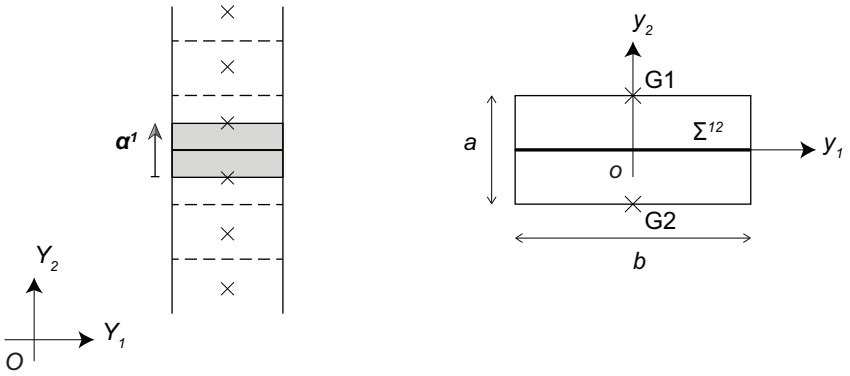

Figure 8: Periodic masonry column (left) and the corresponding elementary cell (right).

5.2. Average Cosserat variables

The kinematics of the masonry column is described by piece-wise linear distributions of the displacement and angular displacement velocity fields of the form (12). In this case, and for the elementary cell considered, the map (24) giving the kinematically admissible sets $\left(v_\alpha^{\mathrm{G}J}, \omega^{\mathrm{G}J}\right) \in KA(V_\alpha, \Omega^c)$ yields:

$$KA(V_\alpha, \Omega^c) = \left\{ \left(v_\alpha^{\mathrm{G}J}, \omega^{\mathrm{G}J}\right) | v_\alpha^{\mathrm{G}J} = D_{\alpha 2} y_2^{\mathrm{G}J} + V_\alpha,\ \omega^{\mathrm{G}J} = K_2 y_2^{\mathrm{G}J} + \Omega^c, \forall J = 1, 2 \right\}, \tag{40}$$

with $\alpha = 1, 2$. Similarly, the resulting displacement and angular displacement field distributions (Eq.(25)) read:

$$v_\alpha^J(\boldsymbol{y}) = \Gamma_{\alpha 2} y_2^{\mathrm{G}J} + V_\alpha - e_{\alpha\beta}\left[K_2 y_2^{\mathrm{G}J}\left(y_\beta - y_\beta^{\mathrm{G}J}\right) + \Omega^c y_\beta\right]$$
$$\omega^J(\boldsymbol{y}) = K_2 y_2^{\mathrm{G}J} + \Omega^c, \forall \boldsymbol{y} \in B^J. \tag{41}$$

The above equations consist in a limited number of terms of macroscopic deformation. With respect to the general form (25), where all the Cosserat deformation measures $(\Gamma_{\alpha\beta}, K_\beta)$ are present, the only available deformations measures in Eq.(41) are $\Gamma_{\alpha 2}$ and K_2. This results from the geometry of the discrete cell. Here, the blocks are arranged following a periodic lattice that is developed along one periodicity vector and the orientation of the interface is perpendicular to this vector. For such configuration, replacing the general form (25) into Eqs.(26)-(27) leads to:

$$\Gamma_{\alpha 1} = 0, \quad K_1 = 0. \tag{42}$$

The remaining deformation measures $(\Gamma_{\alpha 2}, K_2)$ presented in Eq.(41) are produced by combinations of in-plane rigid-body motions (i.e. translations and rotations) of the blocks that compose the cell (see Figure 9). Their expression reads from Eqs.(26)-(27) as follows:

$$\Gamma_{\alpha 2} = D_{\alpha 2} + e_{\alpha 2}\Omega^c, \qquad K_2 = \frac{\omega^{\mathrm{G1}} - \omega^{\mathrm{G2}}}{a}, \tag{43}$$

where:

$$D_{\alpha 2} = \frac{v_\alpha^{\mathrm{G1}} - v_\alpha^{\mathrm{G2}}}{a}. \tag{44}$$

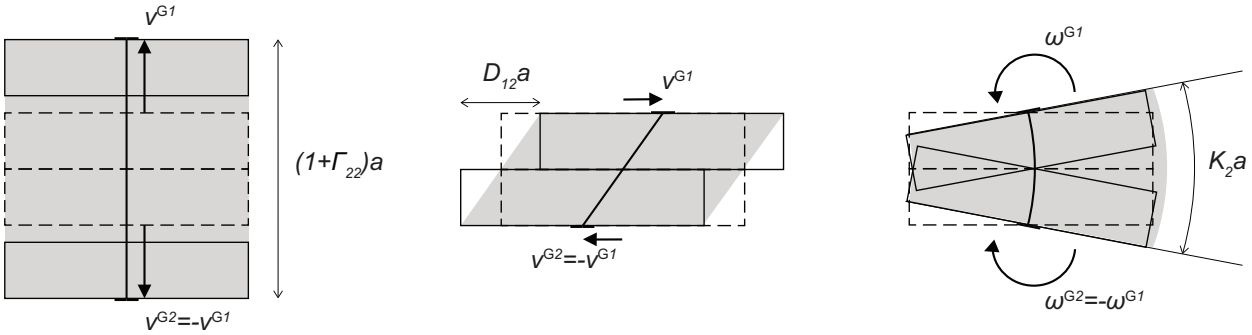

Figure 9: Combinations of rigid-body motions of the blocks producing deformation and curvature states on the elementary cell of a masonry column (in grey), represented as 1D Cosserat deformations (solid lines).

The Cosserat deformations reproduce then the deformation modes of the discrete cell. In particular, blocks' rotations with opposite direction induce the opening of the interface and, consequently, generate curvatures on the cell (Figure 9). On the contrary, the terms V_α and Ω^c denote rigid-body motions of the cell (see Eqs.(30)-(29)). They are provided by combinations of in-plane blocks' motions producing no average deformation on the elementary cell (Figure 10). The first term designates the average rigid-body translations of the cell and is generated by uniform blocks' translations:

$$V_\alpha = \frac{v_\alpha^{\mathrm{G1}} + v_\alpha^{\mathrm{G2}}}{2}. \tag{45}$$

The second term defines the average rigid-body rotation of the cell. It is generated by blocks' rotations having the same direction, which induce the sliding but not the opening of the common interface:

$$\Omega^c = \frac{\omega^{\mathrm{G1}} + \omega^{\mathrm{G2}}}{2}. \tag{46}$$

The Cosserat static quantities are necessarily $T_{\alpha 2}$ and M_2. These forces and couples are provided by distributions of contact stresses r_α^{IJ} along the interface Σ^{12}. The use of the Eqs.(33)-(34) gives directly:

$$T_{\alpha 1} = 0, \quad M_1 = 0, \tag{47}$$

and:

$$T_{\alpha 2} = \frac{1}{b}\int_{-\frac{b}{2}}^{\frac{b}{2}} r_\alpha^{IJ}\mathrm{dL}, \quad M_2 = \frac{1}{b}\int_{-\frac{b}{2}}^{\frac{b}{2}} r_2^{IJ} y_1 \mathrm{dL}. \tag{48}$$

Eq.(47) is a condition for the external facets of the masonry column (for $y_1 = \pm b/2$) to be stress- and couple stress-free. Eq.(48) gives then the overall forces $T_{\alpha 2}$ and the overall moment M_2 of what can be considered a Timoshenko beam model (Mühlhaus et al., 1997).

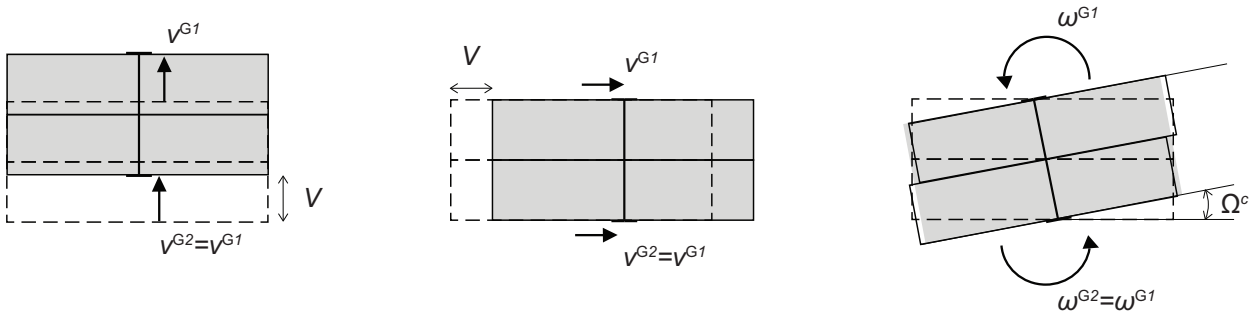

Figure 10: Combinations of rigid-body motions of the blocks producing in-plane rigid-body translations V_α and Cosserat rotations Ω of the elementary cell of a masonry column.

In view of the upscaling, we compute the displacement and angular displacement velocity jumps occurring at the interface Σ^{12}. These jumps read (Eqs.(13),(17)):

$$[\![\boldsymbol{v}]\!]^{12} = a \begin{bmatrix} \Gamma_{12} \\ \Gamma_{22} + y_1 K_2 \end{bmatrix} \tag{49}$$

or equivalently:

$$[\![\omega]\!]^{12} = a K_2, \tag{50}$$

and:

$$[\![\boldsymbol{v}^{\mathrm{G}}]\!]^{12} = a \begin{bmatrix} \Gamma_{12} \\ \Gamma_{22} \end{bmatrix}. \tag{51}$$

5.3. Upscaling

We assume that the strength of the blocks (masonry units) that compose the column is very large compared to that of the interfaces (masonry joints). Failure may then take place only on these latter. The effect of the finite strength of the blocks in the frame of homogenisation of a Cauchy continuum is presented by Stefanou et al. (2015).

For the interface we make use of a Coulomb slip failure criterion. This criterion is classically expressed in the following form:

$$f\left(r_\alpha^{IJ}\right) = |r_\alpha^\tau| - c + r^\sigma \mathrm{Tan}\left[\phi\right] \leq 0. \tag{52}$$

with $r^\sigma = r_\alpha^\sigma \mathrm{n}_\alpha^{IJ}$, c the joint cohesion and ϕ the joint friction angle. Its support function is given in terms of the displacement velocity jumps $[\![v_\alpha]\!]^{IJ}$ and reads (Salençon, 2013):

$$\pi^{IJ} = \pi^{IJ}\left([\![v_\alpha]\!]^{IJ}; \mathrm{n}_\alpha^{IJ}\right) = \frac{c}{\mathrm{Tan}\left[\phi\right]} [\![v_\alpha]\!]^{IJ} \mathrm{n}_\alpha^{IJ}, \tag{53}$$

with $\pi^{IJ} < \infty$ if:

$$[\![v_\alpha]\!]^{IJ} \mathrm{n}_\alpha^{IJ} \geq \left|[\![v_\alpha]\!]^{IJ}\right| \mathrm{Sin}\left[\phi\right], \tag{54}$$

and n_α^{IJ} the unit vector normal to the interface considered. Eq.(54) is called *relevance condition* (Salençon, 2013). From a physical point of view, in a rigid-plastic formulation as the one followed herein, this conditions corresponds to a kinematic constraint establishing the impenetrability between the blocks (see Figure 11). From a mechanical point of view, it assures that the plastic dissipation is finite at every point of the interface, see Eq.(36).

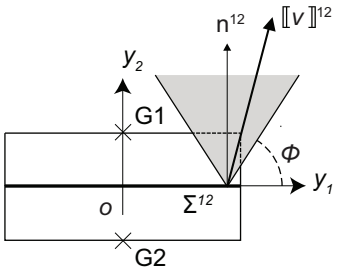

Figure 11: Displacement jump across the interface of the periodic elementary cell of a masonry column, falling within the Coulomb friction cone. Condition for interface failure is that the displacement jump falls inside this cone.

With these definitions, Eqs.(35) and (37) yields:

$$T_{22}\Gamma_{22} + T_{12}\Gamma_{12} + M_2 K_2 \leq \frac{1}{ab}\int_{-\frac{b}{2}}^{+\frac{b}{2}} \pi^{12}\left(\llbracket \boldsymbol{v} \rrbracket^{12}; \mathbf{n^{12}}\right) \mathrm{d}y_1 . \tag{55}$$

Using Eq.(49), one obtains:

$$\pi^{12}\left(\llbracket \boldsymbol{v} \rrbracket^{12}; \mathbf{n^{12}}\right) = \frac{c}{\mathrm{Tan}\left[\phi\right]} a \left(\Gamma_{22} + y_1 K_2\right). \tag{56}$$

Integrating over the interface, Eq.(55) becomes:

$$\left(T_{22} - \frac{c}{\mathrm{Tan}\left[\phi\right]}\right)\Gamma_{22} + T_{12}\Gamma_{12} + M_2 K_2 \leq 0. \tag{57}$$

It is worth pointing out that, at this stage, no failure condition has been explicitly formulated in terms of the angular displacement velocity jumps $\llbracket \omega \rrbracket^{IJ}$ (cf. Trovalusci and Masiani (2003)). The Coulomb slip criterion is expressed only in terms of the displacement jumps $\llbracket v_\alpha \rrbracket^{IJ}$. It is the same criterion with the one originally considered by de Buhan and de Felice (1997) for the homogenisation of masonry panels, with the important exception that now $\llbracket v_\alpha \rrbracket^{IJ}$ is produced by both the relative translations and the relative rotations occurring between the blocks. Indeed, in the case of the Cauchy continuum, Eq.(51) would be used instead of Eq.(49) and Eq.(50) would be omitted.

The consequences of this change emerge in the formulation of the homogenised strength criterion. In fact, looking at Eq.(57), one can state that the homogenised failure criterion is calculated among *all* the $KA(V_\alpha, \Omega^c)$ set of kinematics, associated to the following stresses and couples:

$$T^{'}_{\alpha 2} = \left(T_{\alpha 2} - \frac{c}{\mathrm{Tan}\left[\phi\right]}\delta_{\alpha 2}\right), \quad M^{'}_2 = M_2$$

These kinematics, in order to be relevant in the formulation of the maximum plastic dissipation (56), must respect condition (54), reading in this case:

$$-\Gamma_{22} + \mathrm{Tan}\left[\phi\right]|\Gamma_{12}| - y_1 K_2 \leq 0, \forall y_1 \in \left[-\frac{b}{2}, +\frac{b}{2}\right]. \tag{58}$$

As Eq.(58) is linear, it needs to be verified only at the extreme points of the cell's interface, i.e. at $y_1 = \pm b/2$. This leads to the following four distinct inequalities:

$$H_{1-4}\left(\Gamma_{\alpha 2}, K_2\right) = -\Gamma_{22} \pm \mathrm{Tan}\left[\phi\right]\Gamma_{12} \pm \frac{\mathrm{b}}{2} K_2 \leq 0. \tag{59}$$

These inequalities forms a conical region that is bounded by four intersecting planes of equation $H_{1-4} = 0$ and with the apex in the origin of the axes (Figure 12-Figure 13). Condition for failure of the cell is then that

the macroscopic deformation state falls inside the depicted domain. The set of stresses and couple stresses for which cell failure may occur (yield criterion), is also a cone. This cone is generated in the Cosserat generalised stress space $(T_{\alpha 2}, M_2)$ by the normality rule (Naghdi and Trapp (1975); Lee (1995)) applied at the apex of (59) (see also de Buhan and de Felice (1997)). The resulting homogenised strength domain $G^{c,hom}$ is then the convex hull of the normal vectors produced by the normality rule. In this case, it is given by the following four surfaces:

$$F_{1,2}\left(T_{\alpha 2}, M_2\right) = \pm T_{12} + \mathrm{Tan}\left[\phi\right]\left(T_{22} - \frac{c}{\mathrm{Tan}\left[\phi\right]}\right) \leq 0$$
$$F_{3,4}\left(T_{\alpha 2}, M_2\right) = \pm\frac{2}{b}M_2 + \left(T_{22} - \frac{c}{\mathrm{Tan}\left[\phi\right]}\right) \leq 0. \tag{60}$$

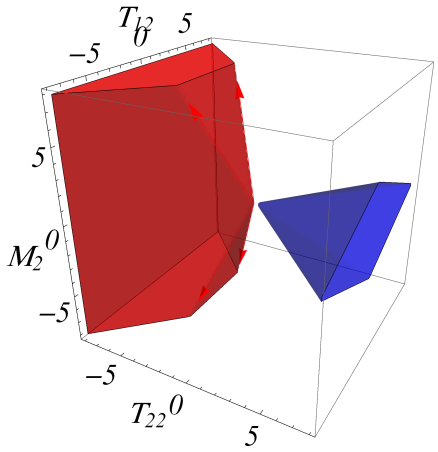

Figure 12: In blue: intersecting planes of Equation (59). In red: intersecting planes of Equation (60), giving the strength domain for the masonry column in the space of the generalised Cosserat stresses $(T_{\alpha 2}, M_2)$.

5.4. Discussion

In this paragraph, we focus on: a) the contribution of the Cosserat model in the determination of the strength domain of the masonry column, and b) the effect of the choice of the cell on the computed strength.

For the first purpose, it is useful to express the macroscopic couple stress M_2 as: $M_2 = (b/2)\zeta T_{22}$, where ζ is the normalized distance from the center of the column cross section. The homogenised strength criterion (60) takes the following alternative form:

$$F_{1,2}\left(T_{\alpha 2}, \zeta\right) = \pm T_{12} + \mathrm{Tan}\left[\phi\right]\left(T_{22} - \frac{c}{\mathrm{Tan}\left[\phi\right]}\right) \leq 0$$
$$F_{3,4}\left(T_{\alpha 2}, \zeta\right) = \pm\zeta T_{22} + \left(T_{22} - \frac{c}{\mathrm{Tan}\left[\phi\right]}\right) \leq 0, \tag{61}$$

with $\zeta \leq |1|$ when T_{22} falls into the section, and $\zeta > |1|$ otherwise. The resulting domain is plotted in Figure 14, in the $(T_{12} - T_{22})$-stress space and for different values of eccentricity ζ. It is worth emphasizing the fact that the Coulomb slip criterion (53) considered as failure condition at the interface level (masonry joints) is retrieved at the macroscopic scale, as a failure condition for the whole cell (masonry column). This condition is described by Eq.(61)-1, and a similar expression can be recovered also when homogenisation is carried out with the use of a simple Cauchy continuum, i.e. for $\zeta = 0$ (Figure 14-left). The expression has the same form, but it is expressed in terms of the macroscopic deformation $D_{(\alpha 2)}$ instead of $\Gamma_{\alpha 2}$. On the contrary, the effects of considering a Cosserat continuum are visible when also the second condition

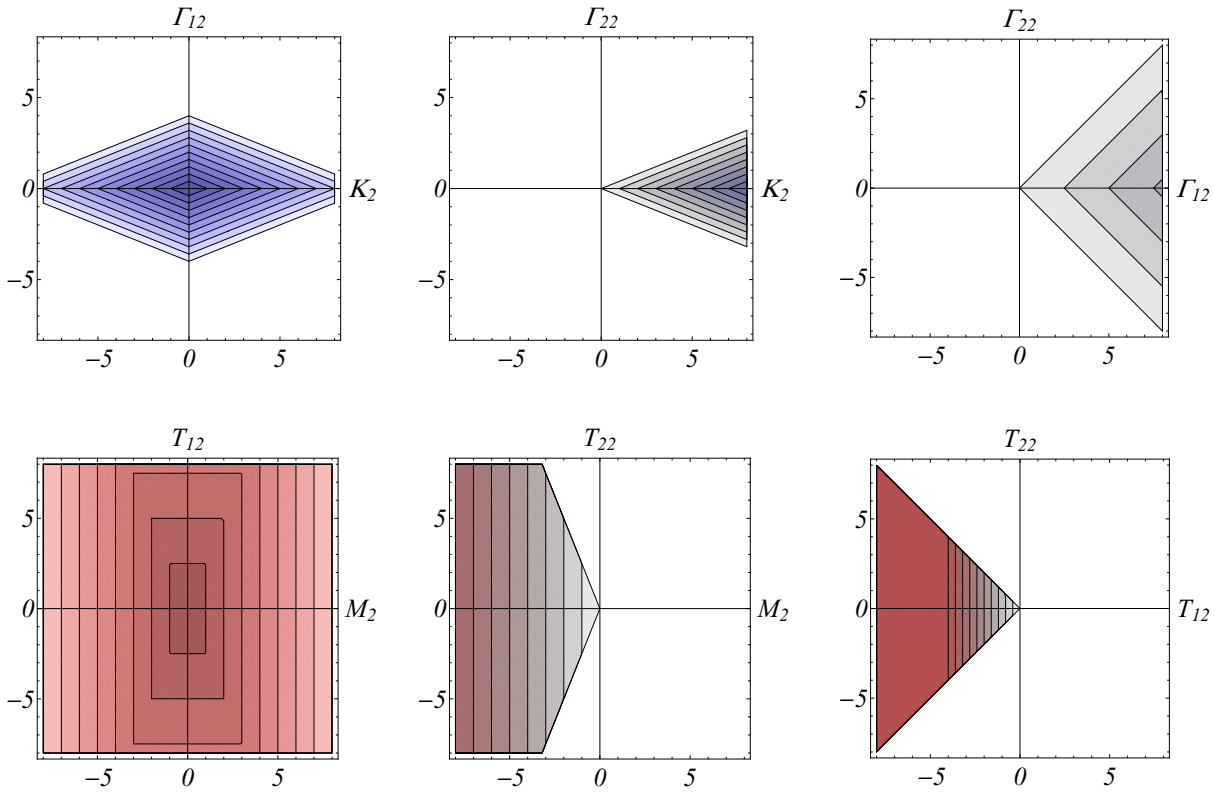

Figure 13: Sections of the intersecting planes of Equation (59) (top) and the intersecting planes of Equation (60) (bottom), giving the strength domain for the masonry column in the space of the generalised Cosserat stresses $(T_{\alpha 2}, M_2)$

(Eq.(61)-2) is involved, i.e. for $\zeta \neq 0$. In such case (Figure 14-right), the presence of moments M_2 (visible when blocks rotate) limits considerably the tensile (T_{22}) and shear (T_{12}) strength. Consistently, the overall strength capacity of the column is reduced.

For the second purpose, it is worth emphasizing that Eqs.(26)-(34) associate the macroscopic (upscaled) generalised deformation and stress quantities with the displacements and forces of the discrete system. Choosing a different cell, as for instance a larger one (as shown in Figure 15), modifies the specific expressions given in Eqs.(42)-(44). In particular, those related to the relative deformations become:

$$\Gamma_{\alpha 1} = 0, \quad \Gamma_{\alpha 2} = D_{\alpha 2} + e_{\alpha 2}\Omega^c, \qquad K_1 = 0, \quad K_2 = \frac{\omega^{\mathrm{G1}} - \omega^{\mathrm{G5}}}{4a},$$

with:

$$D_{\alpha 2} = \frac{v_\alpha^{\mathrm{G1}} - v_\alpha^{\mathrm{G5}}}{4a}, \quad \Omega^c = \frac{\omega^{\mathrm{G1}} + \omega^{\mathrm{G5}}}{8a} + \frac{\omega^{\mathrm{G2}} + \omega^{\mathrm{G3}} + \omega^{\mathrm{G4}}}{4a}.$$

Comparing the above expressions of the Cosserat generalised displacements and deformations with the corresponding ones of the smaller elementary cell, we notice that their physical meaning changes. In the case of the larger cell, they represent an average over more blocks, which leads to loose deformation modes of shorter wavelengths (Figure 15). In this sense, the choice of a smaller elementary cell provides a finer description of the relative generalised displacements of the microstructure constituents, while a larger one smears them out. This justifies also why Cosserat continuum is better adapted for mono-atomic lattices. For poly-disperse discrete media, this continuum medium is expected to give poor results (as well as Cauchy

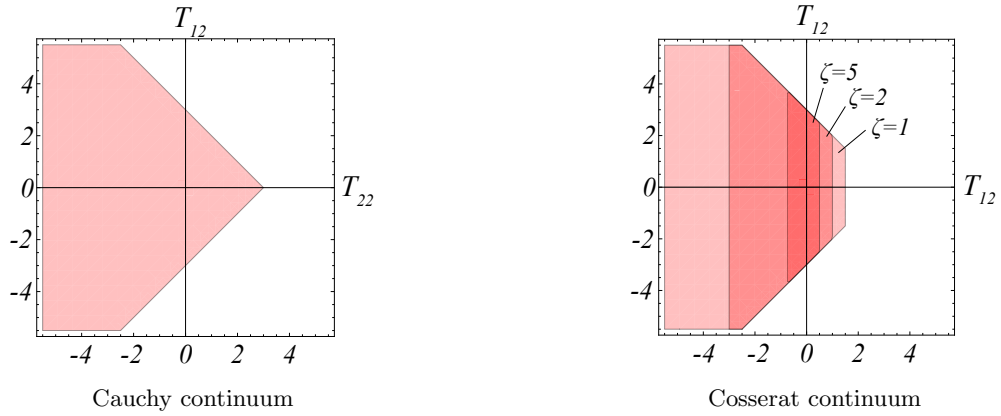

Figure 14: Representation of the homogenised strength domain for the masonry column in the space of the generalised stresses (T_{12}, T_{22}). Strength domain for $\zeta = 0$ (Cauchy continuum) and for $\zeta \neq 0$ (Cosserat continuum).

continuum) and higher order continua should be used (Stefanou et al., 2010). However, this exceeds the scope of the present paper.

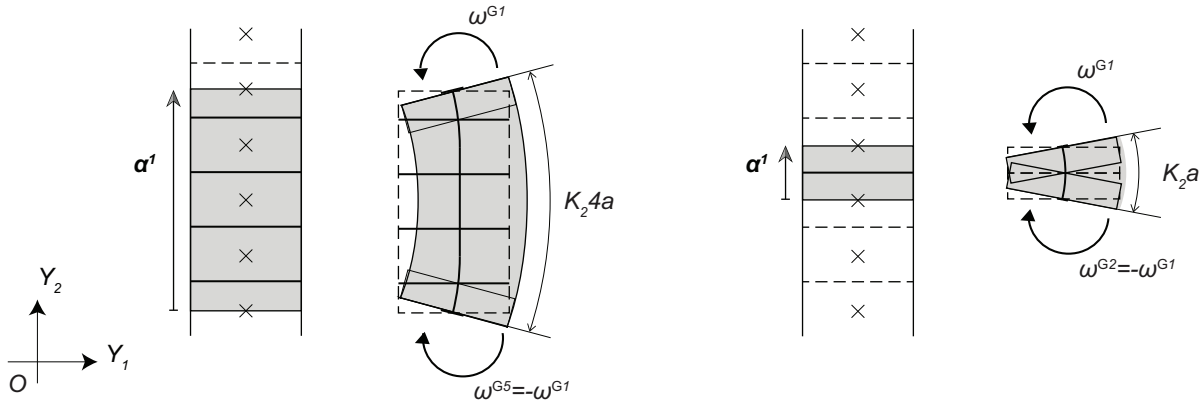

Figure 15: Curvature state produced by the elementary cell larger than B (left) in contrast with the curvature state produced by the elementary cell B (right).

The finer representation of the kinematics of the microstructure with the smaller cell is reflected on the overall computed strength domain. Indeed, when considering elementary cells larger than B, containing a generic number of interfaces $N_\Sigma \geq 1$ (Figure 16), the resulting homogenised yield criteria become:

$$F_{1,2}\left(T_{\alpha 2}, M_2, N_\Sigma\right) = \pm T_{12} + \mathrm{Tan}\left[\phi\right]\left(T_{22} - \frac{c}{\mathrm{Tan}\left[\phi\right]}\right) \leq 0$$
$$F_{3,4}\left(T_{\alpha 2}, M_2, N_\Sigma\right) = \pm\frac{2}{b}\frac{1}{1 + m\ \mathrm{Tan}\left[\phi\right]} M_2 + \left(T_{22} - \frac{c}{\mathrm{Tan}\left[\phi\right]}\right) \leq 0, \tag{62}$$

where $m = (N_\Sigma - 1)a/b$ and a/b is the block aspect ratio. The above expressions show that taking into account larger cells that contain more blocks leads to an enlargement of the homogenised strength domain (Figure 16). In the frame of the kinematic approach of limit analysis, where upper bounds of $G^{c,hom}$ are researched, this results in a worse estimation of the strength capacity of masonry. This is an interesting, but not unexpected result, if one considers that the kinematics of the Cosserat continuum captures the kinematics of the larger cells only in average sense, as discussed above. It is also worth noticing that the increase of strength due to the cell's size is only related to the couple stress M_2 (Eq.(60)-2). This is a

consequence of the fact that the Cosserat curvature is related to the internal length of the microstructure, and that the cell with fewer blocks represents better the relative rotations (Figure 15). On the contrary, the terms related to the tensile and shear forces are not affected by the choice of the cell in this example. Similar considerations hold for more complicated discrete systems as the masonry wall presented in the next section. However, compared to the present example, the algebraic manipulations become more complex for illustrating the effect of the choice of the elementary cell in analytical form.

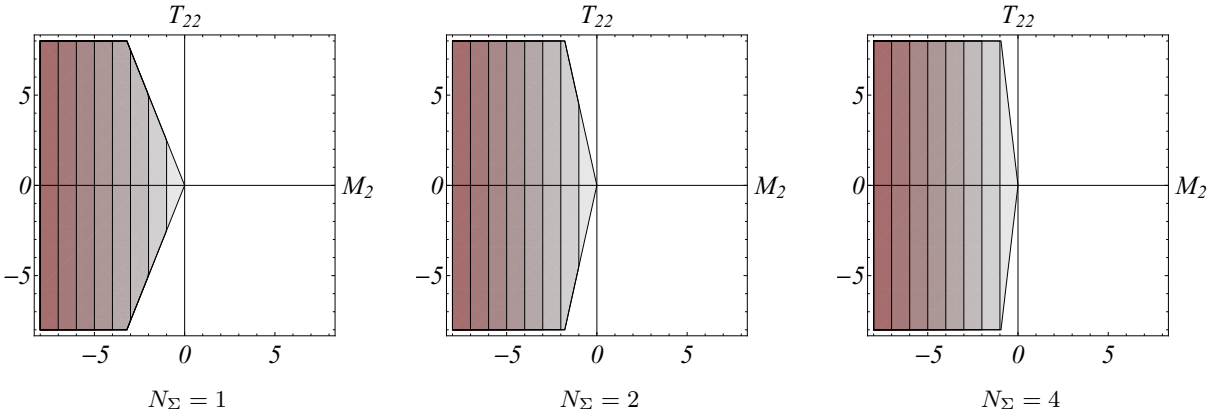

Figure 16: Effect of the size of the cell on the computed strength domain.

6. Application to masonry walls

6.1. Geometry

We consider a masonry wall in which rectangular blocks are disposed according to a generic running bond periodic pattern (Figure 17). In such configuration, periodicity is described by two vectors: $\boldsymbol{\alpha^1} = b\mathbf{e_1} + 0\mathbf{e_2}$ and $\boldsymbol{\alpha^2} = \eta b\mathbf{e_1} + a\mathbf{e_2}$,. The resulting elementary cell is denoted with A. Its area is $|A| = |\boldsymbol{\alpha^1} \times \boldsymbol{\alpha^2}| = ab$, where a and b designate respectively the height and the width of the blocks. The overlap between the blocks is described by ηb, with the parameter $\eta \in [0, 1/2]$. The stack bond and the classic $(1/2)$ running bond patterns are special cases of the considered pattern. They are retrieved respectively for $\eta = 0$ and for $\eta = 1/2$ (Figure 18).

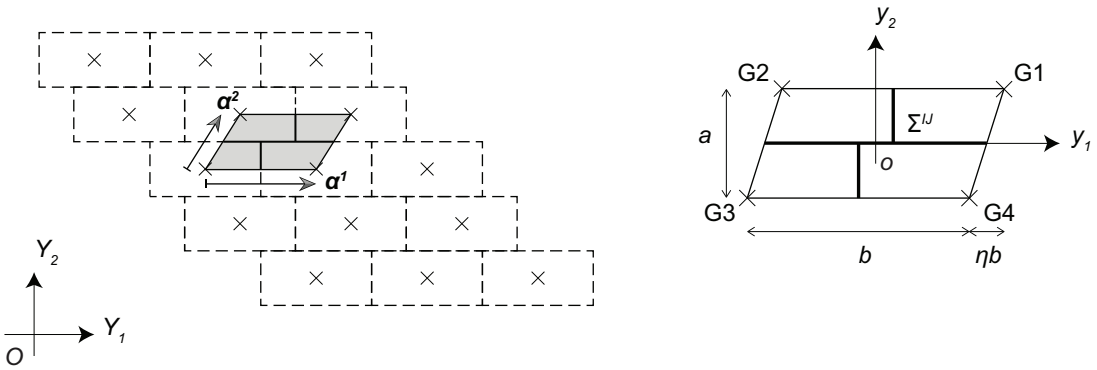

Figure 17: Periodic masonry wall with generic running bond pattern (left) and the corresponding elementary cell (right).

The cell consists of 4 blocks. The position of the centre of mass of each block is expressed with respect

to a local reference system (o, y_1, y_2), attached to the centre of the cell (Figure 17):

$$\begin{aligned}
\boldsymbol{y}^{\mathbf{G1}} &= (1+\eta)\,\frac{b}{2}\mathbf{e_1} + \frac{a}{2}\mathbf{e_2} \\
\boldsymbol{y}^{\mathbf{G2}} &= -(1-\eta)\,\frac{b}{2}\mathbf{e_1} + \frac{a}{2}\mathbf{e_2} \\
\boldsymbol{y}^{\mathbf{G3}} &= -(1+\eta)\,\frac{b}{2}\mathbf{e_1} - \frac{a}{2}\mathbf{e_2} \\
\boldsymbol{y}^{\mathbf{G4}} &= (1-\eta)\,\frac{b}{2}\mathbf{e_1} - \frac{a}{2}\mathbf{e_2}.
\end{aligned}$$

The interfaces shared by the blocks are situated and oriented as follows:

$$\begin{aligned}
\boldsymbol{y}^{\mathbf{\Sigma^{14}}} &= y_1\mathbf{e_1} + 0\mathbf{e_2}, \forall y_1 \in \left[\frac{\eta}{2}b, +\frac{b}{2}\right], \quad \mathbf{n^{14}} = \mathbf{e_2} \\
\boldsymbol{y}^{\mathbf{\Sigma^{23}}} &= y_1\mathbf{e_1} + 0\mathbf{e_2}, \forall y_1 \in \left[-\frac{b}{2}, -\frac{\eta}{2}b\right], \quad \mathbf{n^{23}} = \mathbf{e_2} \\
\boldsymbol{y}^{\mathbf{\Sigma^{24}}} &= y_1\mathbf{e_1} + 0\mathbf{e_2}, \forall y_2 \in \left[-\frac{\eta}{2}b, +\frac{\eta}{2}b\right], \quad \mathbf{n^{24}} = \mathbf{e_2} \\
\boldsymbol{y}^{\mathbf{\Sigma^{12}}} &= \frac{\eta}{2}b\mathbf{e_1} + y_2\mathbf{e_2}, \forall y_2 \in \left[0, +\frac{a}{2}\right], \quad \mathbf{n^{12}} = \mathbf{e_1} \\
\boldsymbol{y}^{\mathbf{\Sigma^{43}}} &= -\frac{\eta}{2}b\mathbf{e_1} + y_2\mathbf{e_2}, \forall y_2 \in \left[-\frac{a}{2}, 0\right], \quad \mathbf{n^{43}} = \mathbf{e_1}.
\end{aligned}$$

It is worth noticing that, in the limit for $\eta \to 0$ (stack bond pattern), the interface between the block 2 and the block 4 degenerates into a point: $|\Sigma^{24}| \to 0$. In this case, Σ^{24} must be excluded from the computations.

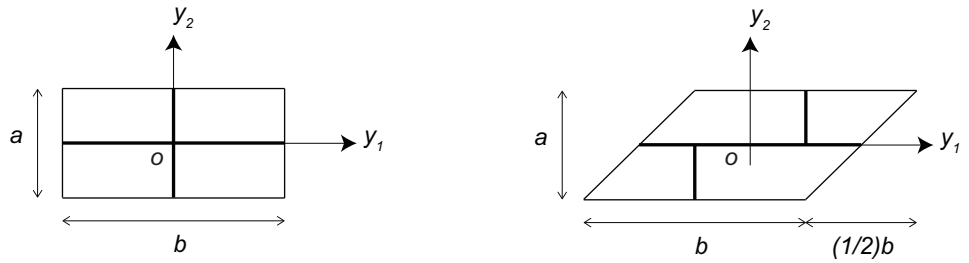

Figure 18: Elementary cells for periodic masonry covered by the cell A. Left: the stack bond pattern, for $\eta = 0$. Right: the classical (1/2) running bond pattern, for $\eta = 1/2$.

6.2. Average Cosserat variables

The elementary cell A is periodic in both local directions. Consequently, the kinematically admissible sets of displacement and angular displacement velocity fields $\left(v_\alpha^{GJ}, \omega^{GJ}\right) \in KA(V_\alpha, \Omega^c)$ follow the general form (24), with $\alpha, \beta = 1, 2$ and $J = 1, \ldots, 4$. The velocity field distributions are of the form (25).

The deformations $(\Gamma_{\alpha\beta}, K_\beta)$ contained in Eq.(25) are produced by combinations of translations and rotations of the blocks that compose the elementary cell. In particular, on the cell A no in-plane Cosserat

deformation measures vanish. The relative deformations are, after Eq.(26):

$$\begin{aligned}
\Gamma_{11} &= \frac{v_1^{\mathrm{G1}} - v_1^{\mathrm{G2}} - v_1^{\mathrm{G3}} + v_1^{\mathrm{G4}}}{2b} + \\
&\quad \frac{a\left(\omega^{\mathrm{G1}} - \omega^{\mathrm{G2}} + \omega^{\mathrm{G3}} - \omega^{\mathrm{G4}}\right)}{8b} \\
\Gamma_{12} &= \frac{(1-\eta)\, v_1^{\mathrm{G1}} + (1+\eta)\, v_1^{\mathrm{G2}} - (1-\eta)\, v_1^{\mathrm{G3}} - (1+\eta)\, v_1^{\mathrm{G4}}}{2a} + \\
&\quad - \frac{\eta\left(\omega^{\mathrm{G1}} - \omega^{\mathrm{G2}} + \omega^{\mathrm{G3}} - \omega^{\mathrm{G4}}\right)}{4} + \Omega^c \\
\Gamma_{21} &= \frac{v_2^{\mathrm{G1}} - v_2^{\mathrm{G2}} - v_2^{\mathrm{G3}} + v_2^{\mathrm{G4}}}{2b} - \Omega^c \\
\Gamma_{22} &= \frac{(1-\eta)\, v_2^{\mathrm{G1}} + (1+\eta)\, v_2^{\mathrm{G2}} - (1-\eta)\, v_2^{\mathrm{G3}} - (1+\eta)\, v_2^{\mathrm{G4}}}{2a} + \\
&\quad - \frac{\left(1-\eta^2\right) b\left(\omega^{\mathrm{G1}} - \omega^{\mathrm{G2}} + \omega^{\mathrm{G3}} - \omega^{\mathrm{G4}}\right)}{8a}.
\end{aligned} \tag{63}$$

The in-plane curvatures write (Eq.(27)):

$$\begin{aligned}
K_1 &= \frac{\omega^{\mathrm{G1}} - \omega^{\mathrm{G2}} - \omega^{\mathrm{G3}} + \omega^{\mathrm{G4}}}{2b} \\
K_2 &= \frac{(1-\eta)\,\omega^{\mathrm{G1}} + (1+\eta)\,\omega^{\mathrm{G2}} - (1-\eta)\,\omega^{\mathrm{G3}} - (1+\eta)\,\omega^{\mathrm{G4}}}{2a}.
\end{aligned} \tag{64}$$

Eqs.(63)-(64) are detailed in Appendix B, for the case of the stack bond and the 1/2 running bond patterns. Regarding the stack bond pattern ($\eta = 0$), an illustration of the Cosserat deformation measures and their connection to the discrete kinematic variables is given in Figure 19. It is worth noticing that the blocks' rotations do not appear only in the expression of the curvatures, but also in that of the relative deformations. In fact, following simple rotations, the blocks can be arranged to form specific geometric configurations that involve the opening of the interfaces and induce average elongations and contractions (Γ_{11}, Γ_{22}) of the cell, see Eq.(63)-1,4. These configurations can take the shape of an hourglass (Figure 19), and cannot be represented by a simple Cauchy continuum, since in that case the macroscopic deformation would be generated by blocks' translations only (see Eq.(28)). The contribution of blocks' rotations in the definition of the relative deformations of the Cosserat continuum is even more apparent when the blocks' overlap is marked, i.e. for increasing η. In such case, blocks' rotations produce also shear deformations (Γ_{12}), see Eq.(63)-2.

The terms V_α and Ω^c represent, as in the case of the column, the average rigid-body kinematics of the cell (Eqs.(30)-(29)). V_α indicates the average rigid-body cell translations (Figure 20-left):

$$V_\alpha = \frac{v_\alpha^{\mathrm{G1}} + v_\alpha^{\mathrm{G2}} + v_\alpha^{\mathrm{G3}} + v_\alpha^{\mathrm{G4}}}{4}. \tag{65}$$

Ω^c equals the average rotation of the blocks of the cell (Figure 20-right):

$$\Omega^c = \frac{\omega^{\mathrm{G1}} + \omega^{\mathrm{G2}} + \omega^{\mathrm{G3}} + \omega^{\mathrm{G4}}}{4}. \tag{66}$$

The stresses $T_{\alpha\beta}$ and couple stresses M_β are computed by using Eq.(33) and (34). They read, respectively:

$$\begin{aligned}
T_{\alpha 1} &= \frac{1}{a}\left(\int_0^{\frac{a}{2}} r_\alpha^{12}\,\mathrm{d}y_2 + \int_{-\frac{a}{2}}^{0} r_\alpha^{43}\,\mathrm{d}y_2\right. \\
&\quad \left. + \int_{\eta\frac{b}{2}}^{\frac{b}{2}} \eta r_\alpha^{14}\,\mathrm{d}y_1 + \int_{-\frac{b}{2}}^{-\eta\frac{b}{2}} \eta r_\alpha^{23}\,\mathrm{d}y_1 - \int_{-\eta\frac{b}{2}}^{\eta\frac{b}{2}} (1-\eta) r_\alpha^{24}\,\mathrm{d}y_1\right) \\
T_{\alpha 2} &= \frac{1}{b}\left(\int_{\eta\frac{b}{2}}^{\frac{b}{2}} r_\alpha^{14}\,\mathrm{d}y_1 + \int_{-\frac{b}{2}}^{-\eta\frac{b}{2}} r_\alpha^{23}\,\mathrm{d}y_1 + \int_{-\eta\frac{b}{2}}^{\eta\frac{b}{2}} r_\alpha^{24}\,\mathrm{d}y_1\right),
\end{aligned} \tag{67}$$

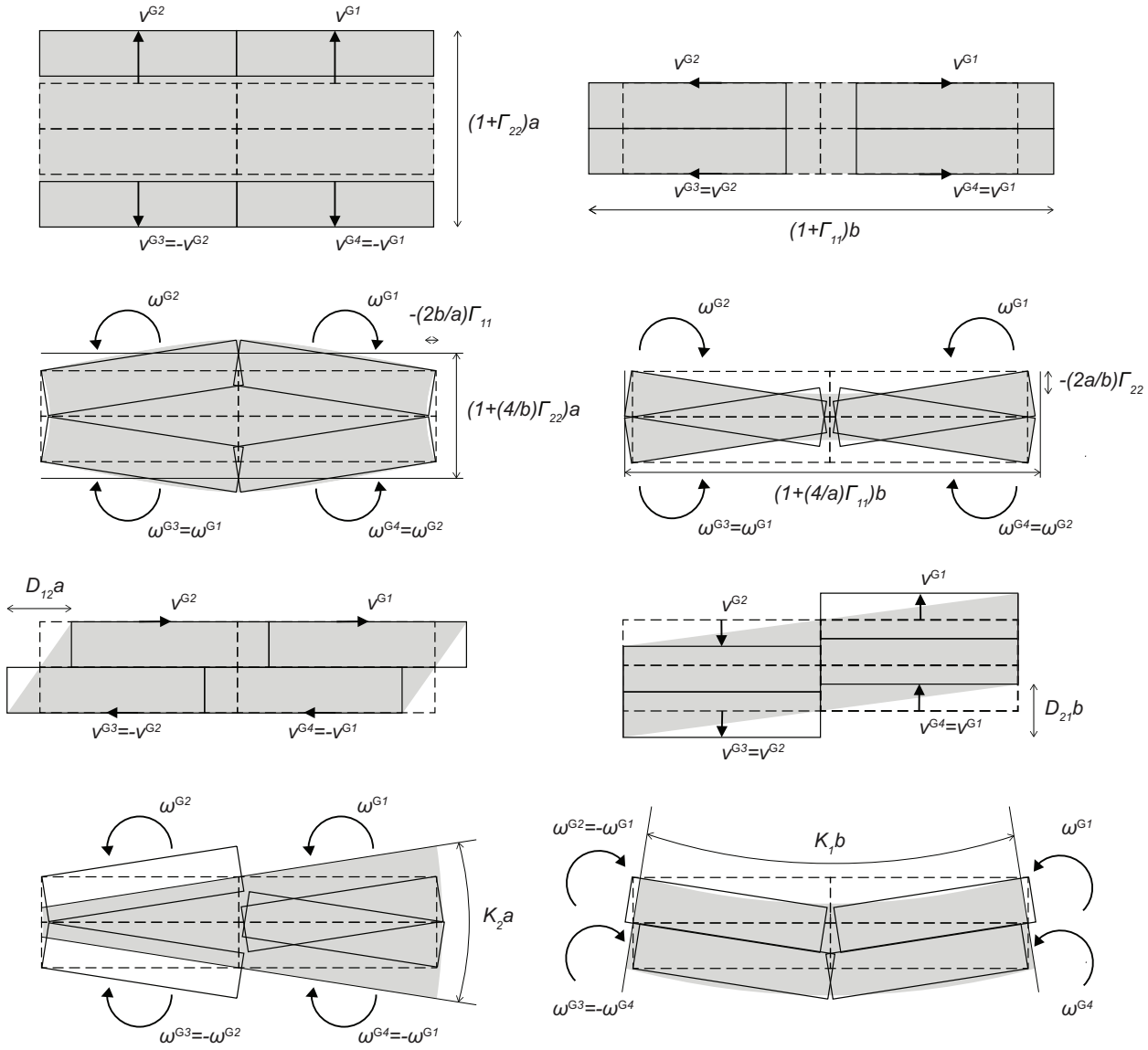

Figure 19: Rigid-body motions of the blocks producing 2D Cosserat deformation and curvature states on the elementary cell of a periodic masonry wall (in grey). Stack bond pattern.

and:

$$M_1 = \frac{1}{a}\left(\int_0^{\frac{a}{2}} \frac{1}{2}\left(-2r_1^{12}y_2 + \eta b r_2^{12}\right)\,\mathrm{d}y_2 + \int_{-\frac{a}{2}}^{0} -\frac{1}{2}\left(2r_1^{43}y_2 + \eta b r_2^{43}\right)\,\mathrm{d}y_2 \right.$$
$$\left. + \int_{\eta\frac{b}{2}}^{\frac{b}{2}} \eta r_2^{14} y_1\,\mathrm{d}y_1 + \int_{-\frac{b}{2}}^{-\eta\frac{b}{2}} \eta r_2^{23} y_1\,\mathrm{d}y_1 - \int_{-\eta\frac{b}{2}}^{\eta\frac{b}{2}} (1-\eta) r_2^{24} y_1\,\mathrm{d}y_1\right)$$
$$M_2 = \frac{1}{b}\left(\int_{\eta\frac{b}{2}}^{\frac{b}{2}} r_2^{14} y_1\,\mathrm{d}y_1 + \int_{-\frac{b}{2}}^{-\eta\frac{b}{2}} r_2^{23} y_1\,\mathrm{d}y_1 + \int_{-\eta\frac{b}{2}}^{\eta\frac{b}{2}} r_2^{24} y_1\,\mathrm{d}y_1\right). \tag{68}$$

Their expression for the stack bond and the classical running bond patterns is given in Appendix C.

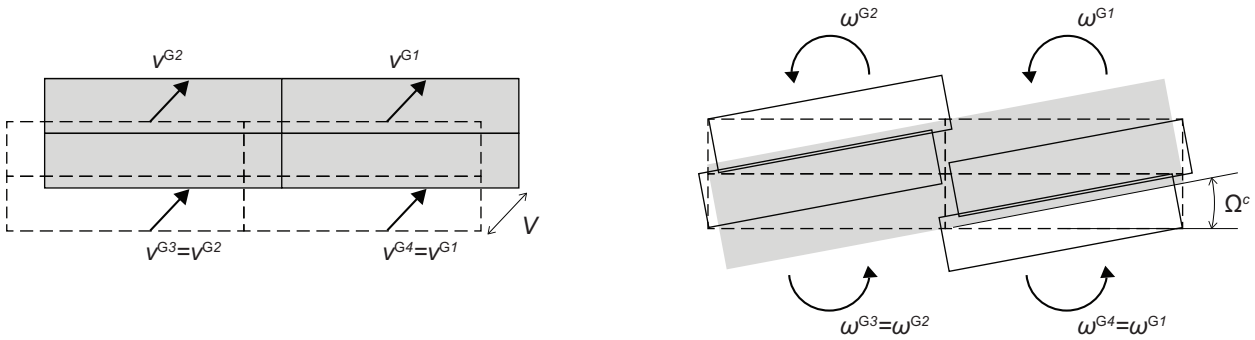

Figure 20: Rigid-body motions of the blocks producing in-plane rigid-body translations V_α and Cosserat rotations Ω^c of the elementary cell of a masonry wall.

The displacement velocity jumps across all the interfaces of the cell A read:

$$\begin{aligned}
[\![\boldsymbol{v}]\!]^{14} &= \begin{bmatrix} \eta b \Gamma_{11} + a\left(\Gamma_{12} + \frac{b}{2}K_1\right) \\ \eta b\left(\Gamma_{21} + (-b + y_1)K_1\right) + a\left(\Gamma_{22} - \frac{b}{2}K_2 + y_1 K_2\right) \end{bmatrix} \\
[\![\boldsymbol{v}]\!]^{23} &= \begin{bmatrix} \eta b \Gamma_{11} + a\left(\Gamma_{12} - \frac{b}{2}K_1\right) \\ \eta b\left(\Gamma_{21} + (b + y_1)K_1\right) + a\left(\Gamma_{22} + \frac{b}{2}K_2 + y_1 K_2\right) \end{bmatrix} \\
[\![\boldsymbol{v}]\!]^{24} &= \begin{bmatrix} (-1+\eta) b \Gamma_{11} + a\Gamma_{12} \\ (-1+\eta) b\left(\Gamma_{21} + y_1 K_1\right) + a\left(\Gamma_{22} + y_1 K_2\right) \end{bmatrix} \\
[\![\boldsymbol{v}]\!]^{12} &= \frac{1}{2} b \begin{bmatrix} 2\Gamma_{11} + (a - 2y_2)K_1 \\ 2\Gamma_{21} - \eta b K_1 - a K_2 \end{bmatrix} \\
[\![\boldsymbol{v}]\!]^{43} &= \frac{1}{2} b \begin{bmatrix} 2\Gamma_{11} - (a + 2y_2)K_1 \\ 2\Gamma_{21} + \eta b K_1 + a K_2 \end{bmatrix}.
\end{aligned} \tag{69}$$

It is worth noticing that Eq.(69) is more general and covers the expression used by Sab (2003); Sab et al. (2007) in the formulation of the in-plane kinematics of their plate models for masonry. In particular, the kinematics considered in the above works are retrieved as s special case of Eq.(69), when curvatures are neglected. The introduction of the curvatures in the description of the in-plane kinematic jumps of the discrete cell is legitimate only in the frame of Cosserat (Stefanou et al., 2008; Salerno and de Felice, 2009) and micromorphic (Stefanou et al., 2010; Stefanou and Sulem, 2012) continua. In these cases, blocks' rotations are appropriately seized by additional deformation measures that are absent in the Cauchy continuum.

6.3. Upscaling

The blocks are considered infinitely resistant, whereas the account of interfaces' failure to shear r_α^τ and to tension r_α^σ is made with reference to a Coulomb slip failure criterion of the form (52). To this purpose, distinction is made between the horizontal interfaces of the cell, representing the masonry bed joints, and the vertical interfaces, representing the masonry head joints. For those two sets of joints, failure results in the use of different values of cohesion and friction (denoted with h and v) and the plastic dissipation at the corresponding interfaces reads (Eq.(53)):

$$\pi^{IJ}\left([\![v_\alpha]\!]^{IJ}; \mathrm{n}_\alpha^{IJ}\right) = \frac{c}{\mathrm{Tan}\left[\phi\right]} [\![v_\alpha]\!]^{IJ} \mathrm{n}_\alpha^{IJ}, \text{ with } \begin{cases} (c,\phi) = (c^h, \phi^h), \text{ for } \Sigma^{14}, \Sigma^{23}, \Sigma^{24} \\ (c,\phi) = (c^v, \phi^v), \text{ for } \Sigma^{12}, \Sigma^{43}, \end{cases} \tag{70}$$

with $\pi^{IJ} < \infty$ if:

$$\begin{cases} [\![v_\alpha]\!]^{IJ} \mathrm{n}_\alpha^{IJ} \geq \left|[\![v_\alpha]\!]^{IJ}\right| \mathrm{Sin}\left[\phi^h\right], \text{ for } \Sigma^{14}, \Sigma^{23}, \Sigma^{24} \\ [\![v_\alpha]\!]^{IJ} \mathrm{n}_\alpha^{IJ} \geq \left|[\![v_\alpha]\!]^{IJ}\right| \mathrm{Sin}\left[\phi^v\right], \text{ for } \Sigma^{12}, \Sigma^{43}. \end{cases} \tag{71}$$

The adoption of distinct interface properties between the bed and the head joints corresponds to the use, in practical applications, of joints with different thickness and strength. In general, the bed joints are thicker than the head joints, and, in many cases, these latter are left unfilled. It is known how this results in an overall reduction of the in-plane strength capacity of masonry (Barth and Marti, 1997; Mojsilović, 2011) and therefore it is taken into account in the computations.

The plastic dissipation on the whole cell is then:

$$\pi^D\left(v_\alpha^{GJ},\omega^{GJ}\right)=\frac{1}{ab}\left(\int_{\eta\frac{b}{2}}^{\frac{b}{2}}\pi^{14}\left(\llbracket\boldsymbol{v}\rrbracket^{14};\mathbf{n^{14}}\right)\mathrm{d}y_1\right.$$
$$+\int_{-\frac{b}{2}}^{-\eta\frac{b}{2}}\pi^{23}\left(\llbracket\boldsymbol{v}\rrbracket^{23};\mathbf{n^{23}}\right)\mathrm{d}y_1+\int_{-\eta\frac{b}{2}}^{\eta\frac{b}{2}}\pi^{24}\left(\llbracket\boldsymbol{v}\rrbracket^{24};\mathbf{n^{24}}\right)\mathrm{d}y_1$$
$$\left.+\int_0^{\frac{a}{2}}\pi^{12}\left(\llbracket\boldsymbol{v}\rrbracket^{12};\mathbf{n^{12}}\right)\mathrm{d}y_2+\int_{-\frac{a}{2}}^{0}\pi^{43}\left(\llbracket\boldsymbol{v}\rrbracket^{43};\mathbf{n^{43}}\right)\mathrm{d}y_2\right),\tag{72}$$

where the displacement jumps $\llbracket v_\alpha\rrbracket^{IJ}$ follow Eq.(69). Using Eq.(70), Eqs.(35) and (37) reduce to:

$$T_{11}^{'}\Gamma_{11}+T_{12}^{'}\Gamma_{12}+T_{21}^{'}\Gamma_{21}+T_{22}^{'}\Gamma_{22}+M_1^{'}K_1+M_2^{'}K_2\leq 0,\tag{73}$$

where we set:

$$T_{11}^{'}=\left(T_{11}-\frac{c^v}{\mathrm{Tan}\left[\phi^v\right]}\right),\quad T_{22}^{'}=\left(T_{22}-\frac{c^h}{\mathrm{Tan}\left[\phi^h\right]}\right),\quad T_{12}^{'}=T_{12},\quad T_{21}^{'}=T_{21},\quad M_\beta^{'}=M_\beta.$$

The homogenised strength criterion is calculated among *all* the $KA\left(\Gamma_{\alpha\beta},K_\beta\right)$ set of kinematics (25), associated to the Cosserat deformations defined above. Conditions (71) need to be verified at every end point of each interface (see Figure 21). Notice that in absence of blocks' rotations, it would be sufficient to verify the relevance condition only at the extreme points of the cell A, i.e. at points P1,...,P4 (Sab, 2003; Sab et al., 2007).

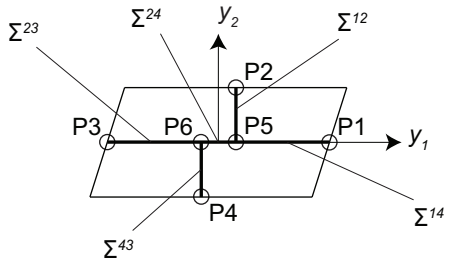

Figure 21: Points of the elementary cell where the relevance condition needs to be verified.

At the points belonging to the horizontal interfaces (bed joints) the relevance condition results in the following 12 conditions:

$$H_{1-8}\left(\Gamma_{\alpha\beta},K_\beta\right)=-a\left(\Gamma_{22}-\epsilon_1\left(1-\epsilon_2\right)\frac{b}{2}K_2\right)$$
$$+\eta b\left(-\Gamma_{21}+\epsilon_1\left(1-\frac{\epsilon_2}{2}\right)bK_1\right)+\epsilon_0\mathrm{Tan}\left[\phi^h\right]\left[\eta b\Gamma_{11}+a\left(\Gamma_{12}+\epsilon_1\frac{b}{2}K_1\right)\right]\leq 0\tag{74}$$

$$H_{9-12}\left(\Gamma_{\alpha\beta},K_\beta\right)=-a\left(\Gamma_{22}+\epsilon_3\frac{\eta b}{2}K_2\right)$$
$$+(1-\eta)b\left(\Gamma_{21}+\epsilon_3\frac{\eta b}{2}K_1\right)+\epsilon_0\mathrm{Tan}[\phi^h]\left[-(1-\eta)b\Gamma_{11}+a\Gamma_{12}\right]\leq 0.\tag{75}$$

At the points belonging to the vertical interfaces (head joints) the relevance condition leads to the following 8 conditions:

$$H_{13-20}\left(\Gamma_{\alpha\beta}, K_\beta\right) = -\left(\Gamma_{11} + \epsilon_4 \frac{a}{2} K_1\right) + \epsilon_0 \mathrm{Tan}[\phi^v]\left[\epsilon_5 \Gamma_{21} + \frac{\eta b}{2} K_1 + \frac{a}{2} K_2\right] \leq 0. \tag{76}$$

The coefficients $\epsilon_0, \epsilon_1, \ldots, \epsilon_5$ take the value -1,0,+1,η according to Table 1.

	Σ^{14}		Σ^{23}		Σ^{24}		Σ^{12}		Σ^{43}	
	P1	P5	P3	P6	P5	P6	P2	P5	P4	P6
ϵ_0	± 1	± 1	± 1	± 1	± 1	± 1	± 1	± 1	± 1	± 1
ϵ_1	1	1	-1	-1						
ϵ_2	1	η	1	η						
ϵ_3					1	-1				
ϵ_4							0	1	0	-1
ϵ_5							-1	-1	1	1

Table 1: Coefficients used in Eqs.(74)-(76).

The inequalities contained in Eqs.(74)-(76) give a convex cone formulated in the space of the generalised Cosserat deformations $(\Gamma_{\alpha\beta}, K_\beta)$ and with its apex falling at the origin of the axes (Figure 22).

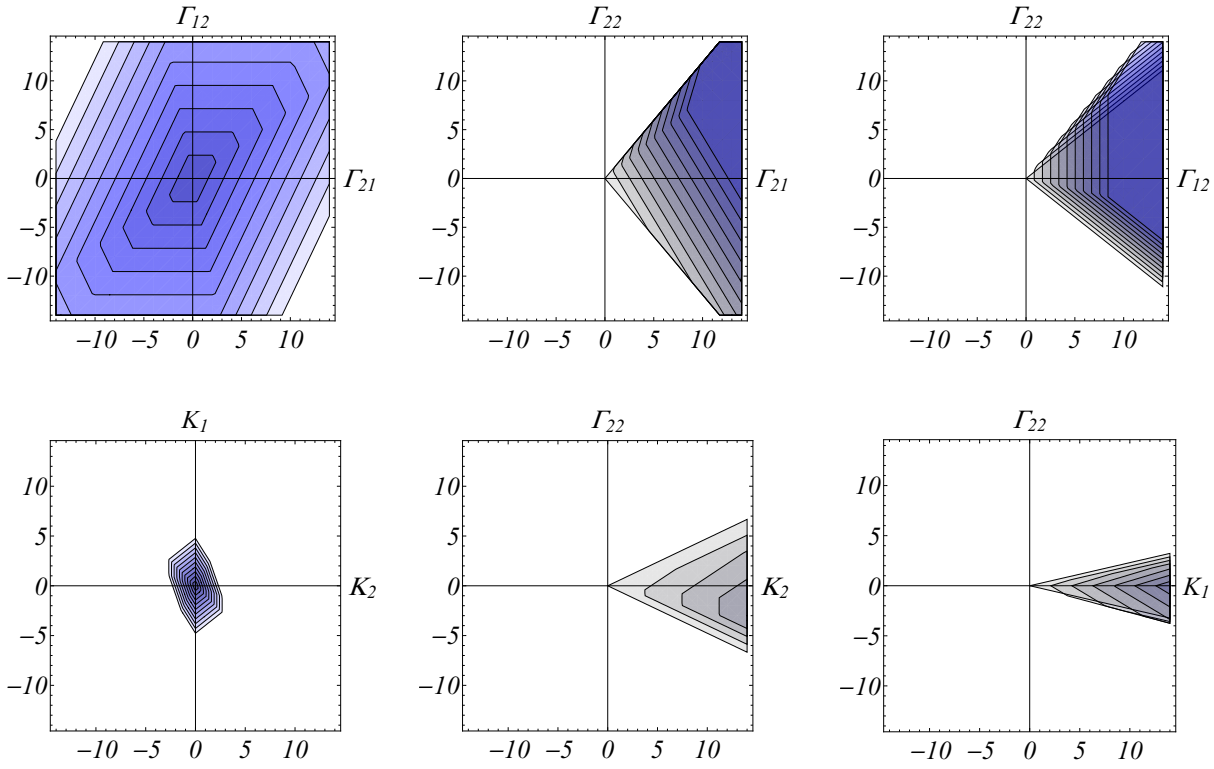

Figure 22: Sections of the computed convex cone in the space of Cosserat deformations (Eqs (74)-(76)). Intersections with $K_1 = K_2 = 0$ (top) and with $\Gamma_{12} = \Gamma_{21} = 0$ $(\Gamma_{11} = \Gamma_{22})$ (bottom). Reference to the 1/2 running bond masonry pattern.

It is possible to retrieve the homogenised strength domain $G^{c,hom}$ as in the case of the column. The normality rule generates a set of normal vectors (Figure 22). The resulting homogenised strength domain

$G^{c,hom}$ is then the region of the generalised Cosserat stresses $(T_{\alpha\beta}, M_\beta)$ enclosed by the convex hull formed by these vectors. Notice that the research of the convex hull gives automatically, i.e. for any given set of deformations, the failure mechanisms producing the minimum plastic dissipation on the discrete cell (upper bound theorem). However, with respect to Section 5, the corresponding yield surfaces are here computed semi-analytically. This is due to the large number of equations and variables.

7. Comparison with existing works and with discrete element simulations

In this section, we show the contribution of the present Cosserat continuum model in the evaluation of the in-plane strength of masonry with respect to other existing works.

It is worth mentioning that a considerable amount of literature is devoted to the modelling of the in-plane strength of masonry. For instance, one may mention the works of Baggio and Trovalusci (1998); Pietruszczak and Ushaksaraei (2003); Mojsilović (2011), among others. Concerning the use of homogenisation (or upscaling) models, other than the aforementioned works one may cite de Buhan and de Felice (1997); Sab (2003); Massart et al. (2004); Milani et al. (2006a,b); Sab et al. (2007); Chettah et al. (2013); Stefanou et al. (2015); Milani and Taliercio (2015). However, a very limited number of works have shown the use of Cosserat medium for the evaluation of masonry strength. Sulem and Mühlhaus (1997) proposed strength criteria for masonry in the framework of plasticity theory formulated for Cosserat materials (see also Besdo (1985); Mühlhaus (1989); Dai et al. (1996)). In their work, masonry was regarded as an assemblage of blocks. The criteria were constructed by considering relevant failure mechanisms at the blocks' level. On the same assumption of masonry as a discrete medium were based the works of Trovalusci and Masiani (2003, 2005). However, in that case the strength criteria were not computed explicitly, but numerically. Addessi et al. (2010) and Addessi and Sacco (2012) developped a numerical homogenisation procedure based on the assumption of masonry as a composite Cauchy material at the microscopic scale. The transition to the Cosserat continuum at the macroscopic scale was made by means of a specific kinematic map (Forest and Sab, 1998). The same map was employed in the work of De Bellis and Addessi (2011).

The works considered in this section for comparison are those of de Buhan and de Felice (1997) and Sulem and Mühlhaus (1997). The first work is considered since, as shown in the previous sections, it gives the theoretical basis for the formulation of the strength domain of masonry in the frame of the Cauchy continuum. The present work represents somehow its extension to the Cosserat continuum. The second work is considered since it contains the first (and only) example of strength domain for masonry formulated in the frame of Cosserat continuum. An additional comparison with discrete element simulations and experimental data is also carried out in this section. The scope of this conclusive comparison is to benchmark the proposed upscaling procedure against full detailed model simulations and experimental tests, of which the Cosserat homogenised model gives an upper bound estimate of the response.

7.1. Comparison with de Buhan and de Felice (1997)

The strength domain resulting from the present work are compared to those obtained within the framework of the Cauchy continuum by de Buhan and de Felice (1997); Sab (2003) and Sab et al. (2007), respectively for classical (1/2) running bond and stack bond patterns.

The domains are represented in the space of the in-plane stresses of the Cauchy continuum, i.e. $\left(T_{11}, T_{(12)}, T_{22}\right)$. In order to highlight the contribution of the Cosserat continuum model within the stress space considered, a parameter β is introduced. Defined as $\beta = T_{[12]}/T_{(12)}$, this parameter allows to control simultaneously all the remaining stress measures contained in the Cosserat medium, namely $\left(T_{[12]}, M_1, M_2\right)$. By means of β, the macroscopic in-plane stresses $T_{\alpha\beta}$ and M_β are expressed as follows:

$$T_{12} = (1+\beta)T_{(12)}, \quad T_{21} = (1-\beta)T_{(12)}, \quad M_1 = M_2 = \frac{ab}{a+b}\beta T_{(12)}. \tag{77}$$

By using the above transformations it is possible to express the domain in function of the Cauchy stresses only, and to trace the Cosserat's terms through the parameter β. The expressions for the stack bond and

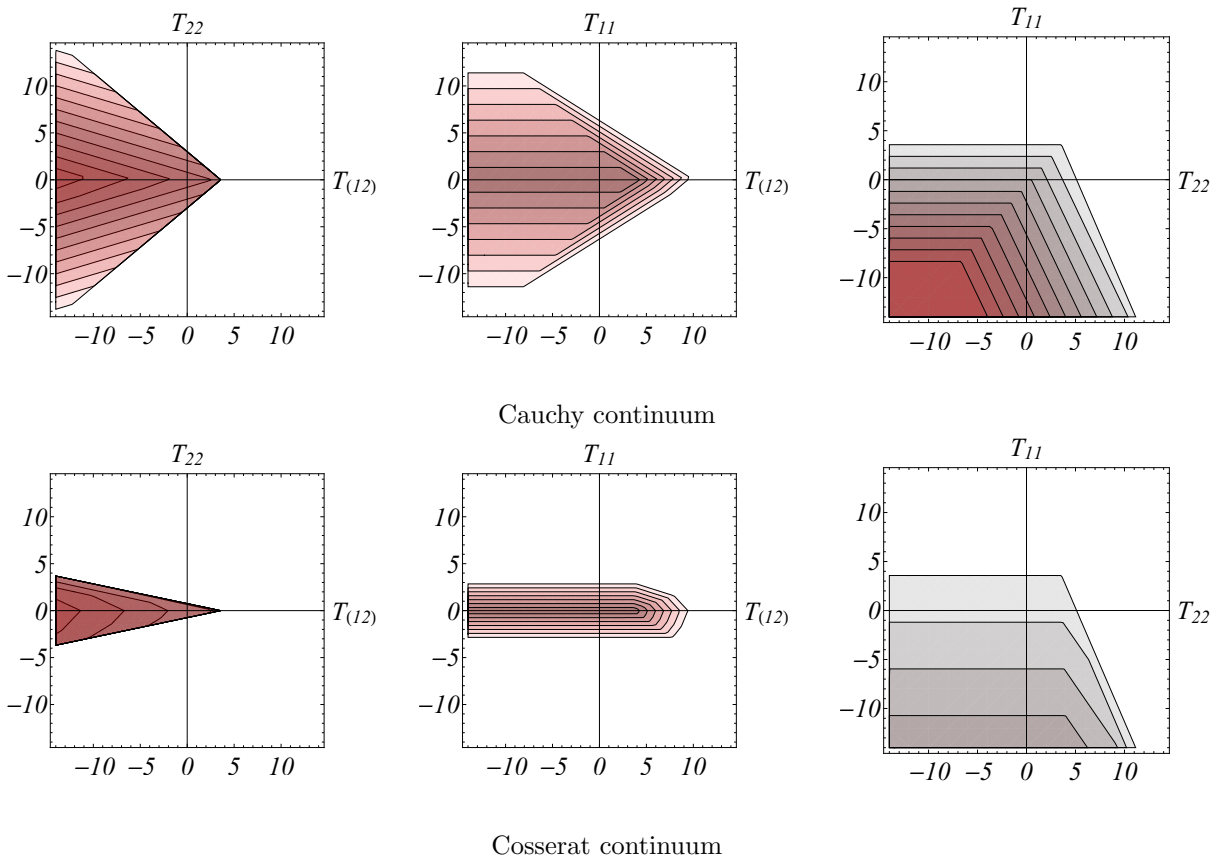

Figure 23: Comparison between the strength domain for the 1/2 running bond masonry pattern, computed for the Cauchy continuum (de Buhan and de Felice, 1997; Sab, 2003) (for $\beta = 0$) and for the Cosserat continuum (present work) ($\beta = 3$).

the running bond patterns are then obtained by imposing $\eta = 0$ and $\eta = 1/2$, respectively (for $\eta = 0$ one has also to neglect Eq.(75) in the computation of the convex hull, see Section 6).

The same friction angle ϕ and cohesion c are considered both for the head and the bed joints. Figure 24 shows the comparison between the strength domain resulting from the present work (Cosserat continuum) and the in-plane strength domains obtained by de Buhan and de Felice (1997); Sab (2003) and Sab et al. (2007) (Cauchy continuum). These letter are retrieved by computing the convex hull, starting from Eqs.(74)-(76) and applying the transformation (77), and by imposing $\beta = 0$. The so-obtained homogenised Cauchy strength domain is then a special case of the present homogenised Cosserat strength domain. In particular, the domain based on Cosserat continuun is contained for the greatest part into the domain referred to the Cauchy continuum. Only a small portion of the Cosserat strength domain falls outside the Cauchy strength domain, as it is visible in the case of the running bond pattern (Figure 24-right). This occurs specifically for $T_{11} > 0$. The role of the terms related to the Cosserat continuum, i.e. the in-plane couples (M_1, M_2) and the non-symmetric stress $T_{[12]}$, is apparent from the comparison. These terms lead to an overall reduction of the masonry strength domain. It is worth noticing that these terms are related to the relative rotation of the blocks.

7.2. Comparison with Sulem and Mühlhaus (1997)

Sulem and Mühlhaus (1997) gave yield criteria for masonry within the framework of a 2D Cosserat continuum theory. Those criteria were constructed by starting from geometrical and physical considerations made directly on the blocks. It resulted in two sets of conditions, representative of both failure mechanisms discussed in Section 3 (Figure 5). The first set was formulated for representing the interface opening

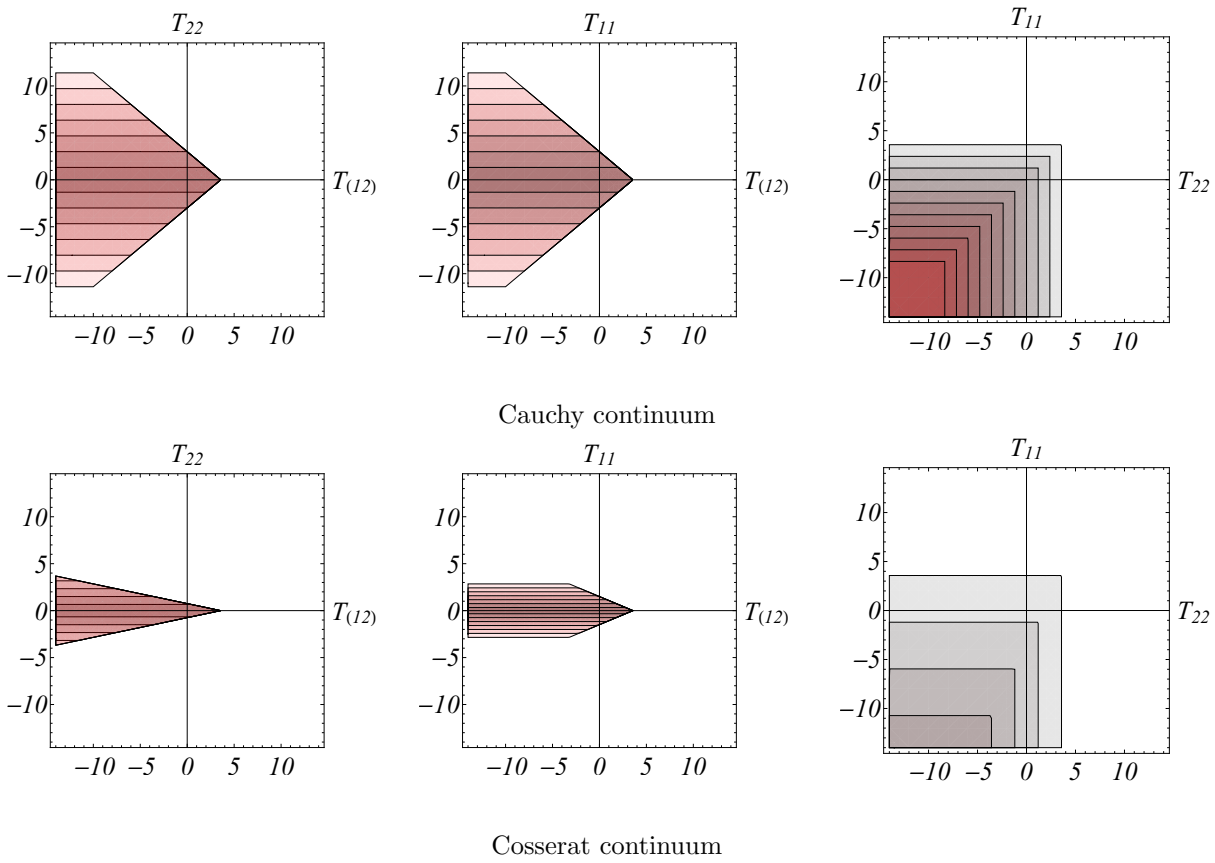

Figure 24: Comparison between the strength domain for the stack bond masonry pattern, computed for the Cauchy continuum (Sab et al., 2007) (for $\beta = 0$) and for the Cosserat continuum (present work) ($\beta = 3$).

mechanism, due to blocks' tilting. Adopting the present notation, it resulted in the following 4 conditions (Sulem and Mühlhaus, 1997):

$$T_{22} \pm \frac{2a}{b} T_{21} - \frac{4}{b} \left| \frac{2a}{b} M_1 \pm M_2 \right| \leq 0. \tag{78}$$

The second set was a cohesion-less Coulomb slip criterion, capable to capture the interface sliding mechanism due to blocks' slip at the bed joints only. It resulted in the following 2 conditions (Sulem and Mühlhaus, 1997):

$$\pm T_{12} + \mathrm{Tan}\left[\phi\right] T_{22} \leq 0. \tag{79}$$

The strength domain for masonry proposed by Sulem and Mühlhaus (1997) is then the region of the generalised Cosserat stress space enclosed by the hyperplanes of equation (78)-(79). In Figure 25 and Figure 26 we show the comparison between this strength domain and the homogenised domain obtained from the present work. The comparison is carried out after having imposed zero joints' cohesion ($c^h = c^v = 0$) and the same friction angle for the head and the bead joints. Two intersections of the strength domains are plotted, one for $M_1 = M_2 = 0$ and one for $T_{12} = T_{21} = 0$. Moreover, for the comparison we impose $T_{11} = 0$ in the homogenised domain. Concerning the intersection with $M_1 = M_2 = 0$ (Figure 25), the depicted Cosserat strength domains are relatively close, with exception to the fact that the homogenised domain exhibits a more pronounced anisotropy. Regarding the intersection with $T_{12} = T_{21} = 0$ (Figure 26), the Cosserat strength domain proposed by Sulem and Mühlhaus (1997) is enclosed by the homogenised

domain obtained here. This is due to the limited number of variables used for the description of the tilting mechanism and present in Eqs.(78)-(79), leading to consider an intersection of the actual strength domain.

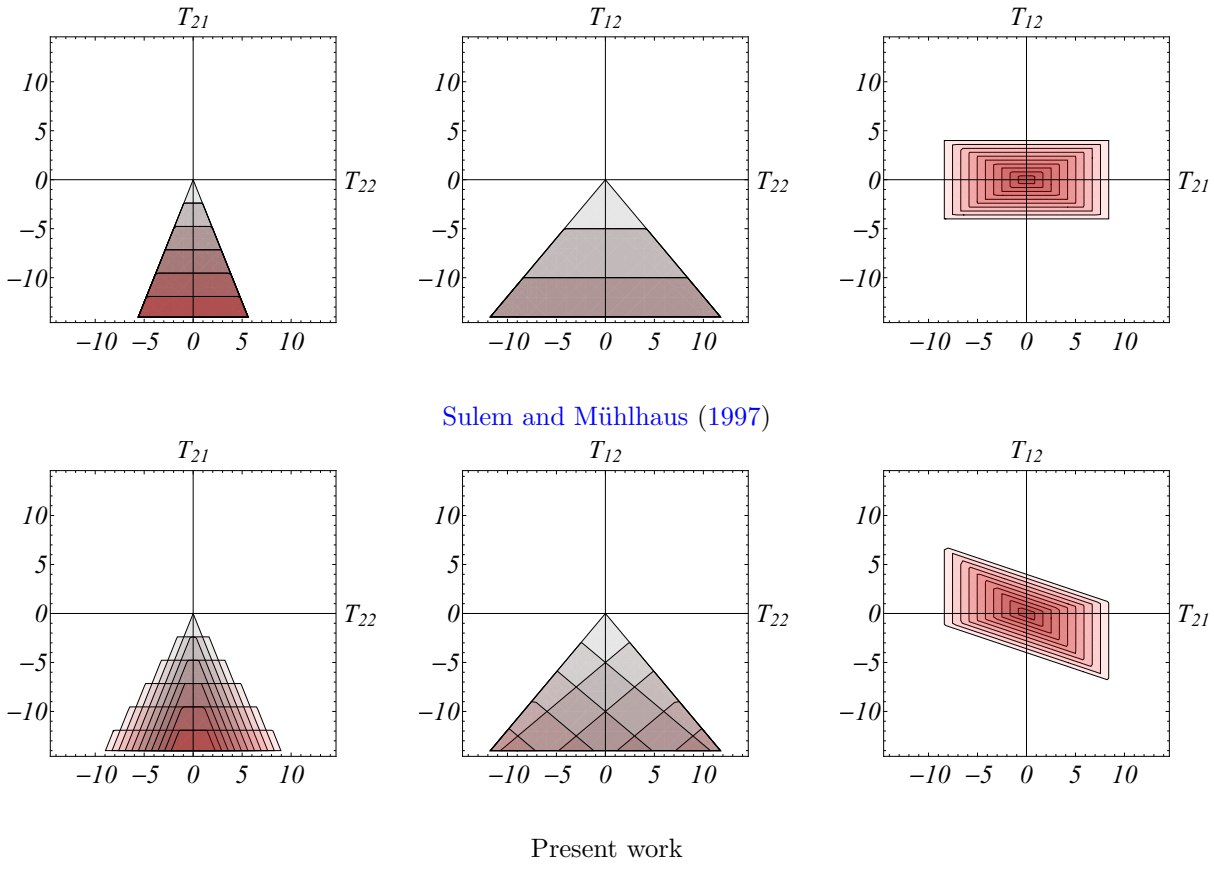

Figure 25: Comparison between the Cosserat strength domain proposed by Sulem and Mühlhaus (1997), Eq.(78)-(79), and the homogenised Cosserat strength domain computed from the present work. Intersections with $M_1 = M_2 = 0$ ($T_{11} = 0$).

7.3. Comparison with discrete element simulations

The numerical benchmark carried out in this section consists in modelling the behaviour of a masonry panel by means of a discrete element model and comparing its response with that given by the homogenised model herein developed. This benchmark represents an interesting example problem, that is typically addressed in the seismic analysis of masonry structures (Petry and Beyer, 2014b). The panel has two openings and has height $H = 3m$, length $L = 6m$ and thickness $t = 0.1m$. Alternate courses of blocks are laid with overlap $\eta = 1/2$. Joints have cohesion $c^h = c^v = 1.2MPa$ and friction angle $\phi^h = \phi^v = 30°$, according to the Coulomb slip criterion considered in the previous sections. The benchmark consists of two steps: first, a vertical load $q = 0.6MPa$ is applied at the top side of the panel. Next, vertical displacements and in-plane rotations are prevented at the top side the panel and a horizontal force F is exerted through a displacement (v) controlled simulation.

Discrete element simulations are carried out by means of 3DEC (Itasca Consulting Group, 2013). The homogenised yield criteria are derived following the procedure presented here and they are implemented in a finite element code specifically developed for Cosserat materials in elasticity, dynamics and multisurface plasticity (Godio et al., 2015, 2016). To this purpose, the elastic behaviour of masonry is represented by the model proposed by Stefanou et al. (2008). Figure 27 shows the comparison between the overall response of the masonry panel provided by the model based on the homogenised Cosserat continuum and that based

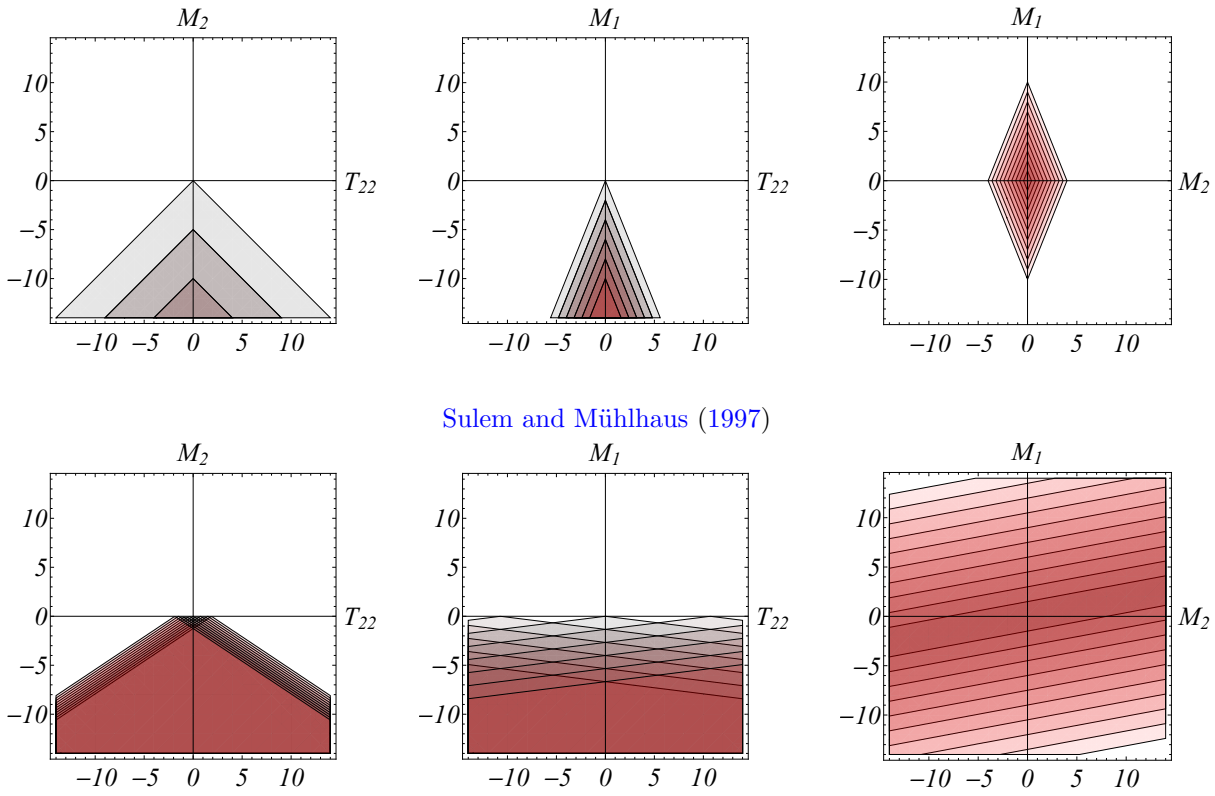

Figure 26: Comparison between the Cosserat strength domain proposed by Sulem and Mühlhaus (1997), Eq.(78)-(79), and the homogenised Cosserat strength domain computed from the present work. Intersections with $T_{12} = T_{21} = 0$ ($T_{11} = 0$).

on the discrete element simulations, in terms of normalized force-displacement curves. The two curves are in agreement, although the one given by the Cosserat model is expectedly slightly steeper than that given by the discrete element model. The capability of the continuum model in representing the discrete element response is also investigated by comparing the development of irreversible plastic deformations in the material, which accompanies the formation of the failure mechanism of the panel. Figure 28 shows how the regions of the model based on Cosserat continuum in which the homogenised yield criteria are activated correspond to the regions of the discrete elements model where the Coulomb slip criterion is violated. This result further assesses the accuracy of the proposed multiscale procedure.

7.4. Comparison with experimental data

The upscaling procedure is benchmarked in this section against the experimental tests carried out by Petry and Beyer (2014a). Masonry walls of height $H = 2.25m$, length $L = 2.01m$ and thickness $t = 0.20m$ are subjected to a constant vertical force and cyclic horizontal displacements up to wall failure. The walls are tested with different shear spans and, for this reason, they undergo shear, flexural and mixed failure modes. Blocks have effective size $0.20 \times 0.31 \times 0.20mm^3$. Mortar joints have friction angle $\phi = 43.2°$ and cohesion $c = 0.27MPa$.

As for the comparison with the discrete element simulations, a finite element model incorporating equivalent elastic properties (Stefanou et al., 2008) and the homogenised yield criteria herein developed is used to model the tests. According to Radenkovich's limit analysis theorems (Salençon, 2013), the walls are modelled by using yield criteria obtained by considering non-zero and zero friction angle, respectively giving

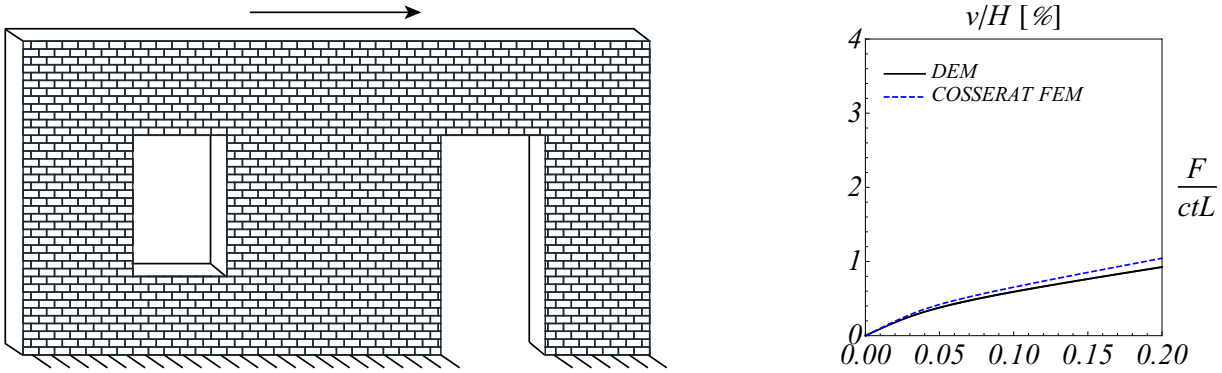

Figure 27: Numerical simulation of a confined masonry panel undergoing shear deformation. Tested configuration (left) and normalized force-displacement curves from discrete element (DEM) and Cosserat finite element (FEM) simulations (right).

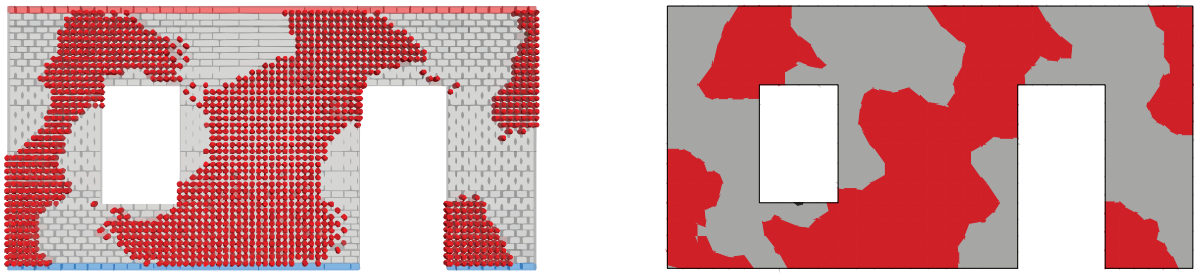

Figure 28: Numerical simulation of a confined masonry panel undergoing shear deformation. Comparison between the pattern of plastic deformation obtained from the discrete (left) and finite element (right) models.

upper and lower bounds to the actual strength capacity of the walls. Following this strategy, the ultimate horizontal load is bounded with, on average, a relative error of approximately ±30% (Table 2).

wall	experimental	upper bound	lower bound
PUP1	187	284	114
PUP2	178	224	114
PUP5	121	164	114

Table 2: Simulation of the experimental tests carried out by Petry and Beyer (2014b). Comparison in terms of ultimate horizontal load (kN).

8. Conclusions

Homogenisation models based on Cosserat (or micropolar) continuum allow to model the mechanical behaviour of discrete media, by incorporating the dominant length scale of the micro-structure. In other words, they permit to take into account not only the geometrical configuration of the inner structure, but also its size and its detailed kinematics. The advantages of micropolar continua are well known nowadays (Mindlin, 1964; Germain, 1973; Vardoulakis and Sulem, 1995; de Borst and Sluys, 1991; Sulem et al., 2011; Sulem and Stefanou, 2016; Godio et al., 2015, 2016; Rezakhani and Cusatis, 2016, among others). However, determining the constitutive parameters for a given micro-structure still remains an open research topic. Various approaches have been proposed in the literature for modelling discrete media in the frame of micropolar elasticity, but only few works for plasticity (de Buhan et al., 1998, 2002) and damage (Rezakhani and Cusatis, 2016).

In this paper, we developed an upscaling procedure for the evaluation of the equivalent in-plane strength of discrete periodic media. The procedure followed here represented somehow the extension to the Cosserat continuum of one initially formulated for the Cauchy continuum, although based on a different upscaling technique. Through this procedure, the relative rotations of the particles and the non-vanishing curvatures of the medium were adequately taken into account.

The procedure was illustrated with regard to a periodic collection of rigid bodies (or blocks). The interaction between the blocks was established at their interfaces by contact. As result of the homogenisation (or upscaling) process, combinations of rigid-body motions of the blocks that compose the discrete medium produced the Cosserat relative deformations and curvatures (see Section 4). Similarly, the non-symmetric stresses and in-plane couples of the equivalent continuum resulted as average values of the contact stress distributions exchanged by the blocks. Due to periodicity, all the computations were made on a preselected elementary cell of the discrete medium. It was noticed that, with respect to the Cauchy continuum, the use of the Cosserat continuum allowed to capture a richer number of deformation modes of this cell. As the number and the type of different deformation modes depended on the size of the cell, the obtained Cosserat continuum also depended on the selection of this latter. However, as it was shown in Section 4 the Cosserat kinematic variables and stress quantities obtain a different meaning for different elementary cells. Besides the kinematics, the difference with the Cauchy continuum also arose in the expression of the power dissipated by the cell, which was better estimated by the Cosserat continuum.

The upscaling procedure was applied to masonry, which is an interesting example of discrete medium due to the presence of interfaces (discontinuities). Yield criteria were obtained by way of the following assumptions made on masonry: a) the strength capacities of the joints were considered far lower than those of the masonry units, regarded as infinitely resistant, and b) masonry joints were considered as interfaces with Coulomb dissipative properties given by joint cohesion and friction angle. Under these assumptions masonry was studied as a discrete assemblage of blocks, which exchange contact stresses and experience rigid-body translations and rotations when masonry undergoes deformation. The in-plane strength of masonry was determined then by identification with an equivalent Cosserat continuum at the macroscopic scale. Even though the same Coulomb failure criterion considered for the Cauchy continuum was used (de Buhan and de Felice, 1997), the expression of the dissipated power retrieved for the Cosserat continuum was different. This change, which held true both for the masonry column (Section 5) and the masonry wall (Section 6), was due to the different kinematics of the two continuum media and led to different forms of the computed strength domains.

The application to masonry allowed to highlight the role of particles' rotations in the strength of a discrete medium. Both the example of the column and of the wall showed that the overall strength capacity of masonry is reduced due to the relative blocks' rotations. The Cosserat continuum correctly captured these effects, in contrast with the Cauchy continuum which did not cover them (see Section 5 and Section 7). Indeed, relative blocks' rotations were related by means of a kinematic map to the in-plane curvatures and the non-symmetric part of the deformation. These deformation measures were conjugate in energy respectively to the in-plane couples (or moments) and the non-symmetric part of the stress tensor of the Cosserat continuum. It is worth mentioning that the presence of moments acting in the plane of the walls is intrinsic in structural problems related to masonry, especially in those related to seismic analyses (Petry and Beyer, 2014b). Aiming at formulating a modelling strategy for masonry in this field, the contribution given by the Cosserat continuum in modelling its strength is therefore of great importance. What was obtained here was an equivalent material, that can be implemented in appropriate finite element codes (Godio et al., 2015, 2016) and used for the advance analysis of masonry structures.

The procedure developed in this paper was presented in rigorous, extensive and general way. Examples of application of the presented procedure are multiple and cover the whole class of discrete periodic media made of particles of the same type. To this class belong, for instance, natural materials with inner micro-structure such as rock assemblies, soils and solid crystals, but also man-made materials as fibre composites, beam lattices and layered structures (Eringen, 1999). It is worth noticing, in conclusion, that the proposed procedure was limited to 2D periodic media. However, it is straightforward to extend this procedure to media with 3D periodic patterns. In that case, a 3D Cosserat continuum will be derived.

Appendix A. Average Cosserat deformations of the discrete cell

The expression of the average cell translation V_α can be demonstrated by introducing Eq.(25)-1 into the form:

$$\begin{aligned}
&\frac{1}{|D|}\left(\sum_{J=1}^{N_D}\int_{B^J} v_\alpha^J \mathrm{dS}\right) = \\
=\ &\frac{1}{|D|}\left(\sum_{J=1}^{N_D}\int_{B^J}\left(\Gamma_{\alpha\beta}y_\beta^{\mathrm{G}J}+V_\alpha-e_{\alpha\beta}\left[K_\gamma y_\gamma^{\mathrm{G}J}\left(y_\beta-y_\beta^{\mathrm{G}J}\right)+\Omega^c y_\beta\right]\right)\mathrm{dS}\right)\\
=\ &V_\alpha+\frac{1}{|D|}\Gamma_{\alpha\beta}\left(\sum_{J=1}^{N_D} y_\beta^{\mathrm{G}J}\left|B^J\right|\right)-\frac{1}{|D|}e_{\alpha\beta}K_\gamma\left(\sum_{J=1}^{N_D} y_\gamma^{\mathrm{G}J}\int_{B^J}\left(y_\beta-y_\beta^{\mathrm{G}J}\right)\mathrm{dS}\right)-\frac{1}{|D|}e_{\alpha\beta}\Omega^c\left(\sum_{J=1}^{N_D}\int_{B^J} y_\beta \mathrm{dS}\right)\\
=\ &V_\alpha+\Gamma_{\alpha\beta}y_\beta^{\mathrm{G}0}-e_{\alpha\beta}\Omega^c y_\beta^{\mathrm{G}0}. \qquad \text{(A.1)}
\end{aligned}$$

When the local reference system is taken at the centre of mass of the elementary cell, the expression reduces to V_α (Eq.(30)). Note that one could obtain the same result also by considering:

$$\frac{1}{|D|}\left(\sum_{J=1}^{N_D}\int_{B^J} v_\alpha^{\mathrm{G}J}\mathrm{dS}\right)=V_\alpha \qquad \text{(A.2)}$$

A proof similar to that shown above for V_α applies for the expression of Ω^c (Eq.(29)). The only difference is that, in this case, Eq.(25)-2 must be considered instead of Eq.(25)-1.

For the demonstration of $D_{\alpha\beta}$ (Eq.(28)) one can write:

$$\begin{aligned}
&\frac{1}{|D|}\left(\sum_{IJ}\int_{\Sigma^{IJ}}[\![v_\alpha^{\mathrm{G}}]\!]^{IJ}\mathrm{n}_\beta^{IJ}\mathrm{dL}\right)=\\
=\ &\frac{1}{|D|}\left(\sum_{IJ}\int_{\Sigma^{IJ}}\left(v_\alpha^{\mathrm{G}I}\mathrm{n}_\beta^{IJ}+v_\alpha^{\mathrm{G}J}\mathrm{n}_\beta^{JI}\right)\mathrm{dL}\right)\\
=\ &\frac{1}{|D|}\left(\sum_{J=1}^{N_D}\int_{\partial B^{J,i}} v_\alpha^{\mathrm{G}J}\mathrm{n}_\beta^J\mathrm{dL}\right)\\
=\ &\frac{1}{|D|}\left(\sum_{J=1}^{N_D}\int_{\partial B^J} v_\alpha^{\mathrm{G}J}\mathrm{n}_\beta^J\mathrm{dL}\right)-\frac{1}{|D|}\left(\sum_{J=1}^{N_D}\int_{\partial B^{J,e}} v_\alpha^{\mathrm{G}J}\mathrm{n}_\beta^J\mathrm{dL}\right), \qquad \text{(A.3)}
\end{aligned}$$

where the boundary of every block ∂B^J is split into the part belonging to the cell interfaces $\partial B^{J,i}$ and the part belonging to the external boundary of the cell: $\partial D=\bigcup_{J=1}^{N_D}\partial B^{J,e}$ and $\partial B^J=\partial B^{J,i}\bigcup\partial B^{J,e}$. After the divergence theorem and by using Eq.(25)-1, the first term gives:

$$\begin{aligned}
&\frac{1}{|D|}\left(\sum_{J=1}^{N_D}\int_{\partial B^J} v_\alpha^{\mathrm{G}J}\mathrm{n}_\beta^J\mathrm{dL}\right)=\\
=\ &\frac{1}{|D|}\left(\sum_{J=1}^{N_D}\int_{B^J} v_{\alpha,\beta}^{\mathrm{G}J}\mathrm{dL}\right)=0, \qquad \text{(A.4)}
\end{aligned}$$

while the second term yields:

$$
\begin{aligned}
& -\frac{1}{|D|}\left(\sum_{J=1}^{N_D}\int_{\partial B^{J,e}} v_\alpha^{GJ}\mathrm{n}_\beta^J \mathrm{dL}\right) = \\
= & -\frac{1}{|D|}\left(\sum_{J=1}^{N_D}\int_{\partial B^{J,e}} \left(D_{\alpha\gamma}y_\gamma^{GJ}+V_\alpha\right)\mathrm{n}_\beta^J \mathrm{dL}\right) \\
= & -\frac{1}{|D|}D_{\alpha\gamma}\left(\sum_{J=1}^{N_D} y_\gamma^{GJ}\int_{\partial B^{J,e}} \mathrm{n}_\beta^J \mathrm{dL}\right) - \frac{1}{|D|}\left(\sum_{J=1}^{N_D} V_\alpha \int_{\partial B^{J,e}} \mathrm{n}_\beta^J \mathrm{dL}\right) = D_{\alpha\beta}.
\end{aligned} \tag{A.5}
$$

The last passage in Eq.(A.5) is proved by the fact that the elementary the cell is enclosed by the periodicity vectors $\boldsymbol{\alpha^1}, \boldsymbol{\alpha^2}$. Therefore, the two outward unit normal vectors of the boundary of the cell ∂D are the covariant vectors of $\boldsymbol{\alpha^1}, \boldsymbol{\alpha^2}$. The same considerations apply for the demonstration of K_β (Eq.(27)), which is not reported here. The demonstration of Eq.(26) for the marcoscopic relative deformation $\Gamma_{\alpha\beta}$ is also similar, and leads to long expressions. For brevity, it will be avoided in the text.

Appendix B. Macroscopic relative deformations and curvatures on the elementary cell A

By making use of Eqs.(26)-(27), and taking into account the rigid-body kinematics of the blocks (Eq.(12)), it is possible to compute the macroscopic Cosserat deformations and curvatures of the cell A in terms of the translational and rotational kinematics of the blocks. As the stack bond and the running bond are common in applications, we give here their expressions.

For the stack bond pattern ($\eta = 0$), the average relative deformations hold:

$$
\begin{aligned}
\Gamma_{11} &= \frac{v_1^{G1}-v_1^{G2}-v_1^{G3}+v_1^{G4}}{2b} + \frac{a\left(\omega^{G1}-\omega^{G2}+\omega^{G3}-\omega^{G4}\right)}{8b} \\
\Gamma_{12} &= \frac{v_1^{G1}+v_1^{G2}-v_1^{G3}-v_1^{G4}}{2a} + \Omega^c \\
\Gamma_{21} &= \frac{v_2^{G1}-v_2^{G2}-v_2^{G3}+v_2^{G4}}{2b} - \Omega^c \\
\Gamma_{22} &= \frac{v_2^{G1}+v_2^{G2}-v_2^{G3}-v_2^{G4}}{2a} - \frac{b\left(\omega^{G1}-\omega^{G2}+\omega^{G3}-\omega^{G4}\right)}{8a},
\end{aligned} \tag{B.1}
$$

and the average curvatures read:

$$
\begin{aligned}
K_1 &= \frac{\omega^{G1}-\omega^{G2}-\omega^{G3}+\omega^{G4}}{2b} \\
K_2 &= \frac{\omega^{G1}+\omega^{G2}-\omega^{G3}-\omega^{G4}}{2a}.
\end{aligned} \tag{B.2}
$$

For the running bond pattern ($\eta = 1/2$), Eqs.(26)-(27) become:

$$
\begin{aligned}
\Gamma_{11} &= \frac{v_1^{G1}-v_1^{G2}-v_1^{G3}+v_1^{G4}}{2b} + \frac{a\left(\omega^{G1}-\omega^{G2}+\omega^{G3}-\omega^{G4}\right)}{8b} \\
\Gamma_{12} &= \frac{v_1^{G1}+3v_1^{G2}-v_1^{G3}-3v_1^{G4}}{4a} - \frac{\omega^{G1}-\omega^{G2}+\omega^{G3}-\omega^{G4}}{8} + \Omega^c \\
\Gamma_{21} &= \frac{v_2^{G1}-v_2^{G2}-v_2^{G3}+v_2^{G4}}{2b} - \Omega^c \\
\Gamma_{22} &= \frac{v_2^{G1}+3v_2^{G2}-v_2^{G3}-3v_2^{G4}}{4a} - \frac{3b\left(\omega^{G1}-\omega^{G2}+\omega^{G3}-\omega^{G4}\right)}{32a},
\end{aligned} \tag{B.3}
$$

and

$$\begin{aligned} K_1 &= \frac{\omega^{\mathrm{G1}} - \omega^{\mathrm{G2}} - \omega^{\mathrm{G3}} + \omega^{\mathrm{G4}}}{2b} \\ K_2 &= \frac{\omega^{\mathrm{G1}} + 3\omega^{\mathrm{G2}} - \omega^{\mathrm{G3}} - 3\omega^{\mathrm{G4}}}{4a}. \end{aligned} \tag{B.4}$$

The various deformation modes for the stack bond pattern (Eqs.(B.1)-(B.2)) are illustrated in Figure 19. For both block patterns, the contribution of the blocks' rotations in the average curvatures (B.2) and (B.4), and in the average deformations (B.1) and (B.3) is apparent. In each case it depends on the aspect ratio of the blocks, a/b.

Appendix C. Macroscopic stresses and couple stresses on the elementary cell A

The expression for the macroscopic stesses and couples stresses as functions of the contact stress distributions on the elementary cell A (Section 6), are retrieved through Eqs.(33)-(34). The equations for the generic running bond pattern are presented in the text (Eqs.(67)-(68)).

For the stack bond pattern ($\eta = 0$) the macroscopic stresses are:

$$\begin{aligned} T_{\alpha 1} &= \frac{1}{a}\left(\int_0^{\frac{a}{2}} r_\alpha^{12}\,\mathrm{d}y_2 + \int_{-\frac{a}{2}}^0 r_\alpha^{43}\,\mathrm{d}y_2\right) \\ T_{\alpha 2} &= \frac{1}{a}\left(\int_0^{\frac{b}{2}} r_\alpha^{14}\,\mathrm{d}y_1 + \int_{-\frac{b}{2}}^0 r_\alpha^{23}\,\mathrm{d}y_1\right), \end{aligned} \tag{C.1}$$

and the macroscopic couple stresses are:

$$\begin{aligned} M_1 &= \frac{1}{a}\left(\int_0^{\frac{a}{2}} -r_1^{12} y_2\,\mathrm{d}y_2 + \int_{-\frac{a}{2}}^0 -r_1^{43} y_2\,\mathrm{d}y_2\right) \\ M_2 &= \frac{1}{b}\left(\int_0^{\frac{b}{2}} r_2^{14} y_1\,\mathrm{d}y_1 + \int_{-\frac{b}{2}}^0 r_2^{23} y_1\,\mathrm{d}y_1\right). \end{aligned} \tag{C.2}$$

For the classical classical running bond pattern ($\eta = 1/2$) they are:

$$\begin{aligned} T_{\alpha 1} &= \frac{1}{a}\left(\int_0^{\frac{a}{2}} r_\alpha^{12}\,\mathrm{d}y_2 + \int_{-\frac{a}{2}}^0 r_\alpha^{43}\,\mathrm{d}y_2\right. \\ &\quad \left. + \int_{\frac{b}{4}}^{\frac{b}{2}} \frac{1}{2} r_\alpha^{14}\,\mathrm{d}y_1 + \int_{-\frac{b}{2}}^{-\frac{b}{4}} \frac{1}{2} r_\alpha^{23}\,\mathrm{d}y_1 + \int_{-\frac{b}{4}}^{\frac{b}{4}} -\frac{1}{2} r_\alpha^{24}\,\mathrm{d}y_1\right) \\ T_{\alpha 2} &= \frac{1}{b}\left(\int_{\frac{b}{4}}^{\frac{b}{2}} r_\alpha^{14}\,\mathrm{d}y_1 + \int_{-\frac{b}{2}}^{-\frac{b}{4}} r_\alpha^{23}\,\mathrm{d}y_1 + \int_{-\frac{b}{4}}^{\frac{b}{4}} r_\alpha^{24}\,\mathrm{d}y_1\right), \end{aligned} \tag{C.3}$$

and:

$$\begin{aligned} M_1 &= \frac{1}{ab}\left(\int_0^{\frac{a}{2}} \frac{1}{4}\left(-4r_1^{12} y_2 + b r_2^{12}\right)\,\mathrm{d}y_2 + \int_{-\frac{a}{2}}^0 -\frac{1}{4}\left(4r_1^{43} y_2 + b r_2^{43}\right)\,\mathrm{d}y_2\right. \\ &\quad \left. + \int_{\frac{b}{4}}^{\frac{b}{2}} \frac{1}{2} r_2^{14} y_1\,\mathrm{d}y_1 + \int_{-\frac{b}{2}}^{-\frac{b}{4}} \frac{1}{2} r_2^{23} y_1\,\mathrm{d}y_1 + \int_{-\frac{b}{4}}^{\frac{b}{4}} -\frac{1}{2} r_2^{24} y_1\,\mathrm{d}y_1\right) \\ M_2 &= \frac{1}{b}\left(\int_{\frac{b}{4}}^{\frac{b}{2}} r_2^{14} y_1\,\mathrm{d}y_1 + \int_{-\frac{b}{2}}^{-\frac{b}{4}} r_2^{23} y_1\,\mathrm{d}y_1 + \int_{-\frac{b}{4}}^{\frac{b}{4}} r_2^{24} y_1\,\mathrm{d}y_1\right). \end{aligned} \tag{C.4}$$

References

Addessi, D., Sacco, E., Mar. 2012. A multi-scale enriched model for the analysis of masonry panels. International Journal of Solids and Structures 49 (6), 865–880.
URL http://linkinghub.elsevier.com/retrieve/pii/S0020768311004069

Addessi, D., Sacco, E., Paolone, A., Jul. 2010. Cosserat model for periodic masonry deduced by nonlinear homogenization. European Journal of Mechanics - A/Solids 29 (4), 724–737.
URL http://linkinghub.elsevier.com/retrieve/pii/S0997753810000410

Baggio, C., Trovalusci, P., 1998. Limit analysis for no-tension and frictional three-dimensional discrete systems. Journal of Structural Mechanics.
URL http://www.tandfonline.com/doi/abs/10.1080/08905459708945496

Bardet, J. P., Vardoulakis, I., Jan. 2001. The asymmetry of stress in granular media. International Journal of Solids and Structures 38 (2), 353–367.

Barth, M., Marti, P., 1997. Tests on Clay Brick Masonry with Dry Head Joints (in German). Report No. 230.

Besdo, D., 1985. Inelastic behavior of plane frictionless block-systems described as Cosserat media. Archives of Mechanics.
URL http://scholar.google.com/scholar?hl=en&btnG=Search&q=intitle:Inelastic+behaviour+of+plane+frictionless+block+systems+described+as+Cosserat+media#0

Cecchi, A., Milani, G., Tralli, A., 2007. A Reissner-Mindlin limit analysis model for out-of-plane loaded running bond masonry walls. International Journal of Solids and Structures 44, 1438–1460.

Cecchi, A., Sab, K., may 2004. A comparison between a 3D discrete model and two homogenised plate models for periodic elastic brickwork. International Journal of Solids and Structures 41 (9-10), 2259–2276.
URL http://linkinghub.elsevier.com/retrieve/pii/S0020768303007224

Charalambakis, N., 2010. Homogenization Techniques and Micromechanics. A Survey and Perspectives. Applied Mechanics Reviews 63 (3), 030803.
URL http://appliedmechanicsreviews.asmedigitalcollection.asme.org/article.aspx?articleid=1399665

Chettah, A., Mercatoris, B., Sacco, E., Massart, T., Sep. 2013. Localisation analysis in masonry using transformation field analysis. Engineering Fracture Mechanics 110, 166–188.
URL http://linkinghub.elsevier.com/retrieve/pii/S0013794413002555

Dai, C., Mühlhaus, H.-B., Meek, J., Duncan Fama, M., Jun. 1996. Modelling of blocky rock masses using the Cosserat method. International Journal of Rock Mechanics and Mining Sciences & Geomechanics Abstracts 33 (4), 425–432.
URL http://linkinghub.elsevier.com/retrieve/pii/0148906295000712

De Bellis, M. L., Addessi, D., 2011. A Cosserat based multi-scale model for masonry structures. International Journal for Multiscale Computational Engineering 9 (5), 543–563.

de Borst, R., Sluys, L., Sep. 1991. Localisation in a Cosserat continuum under static and dynamic loading conditions. Computer Methods in Applied Mechanics and Engineering 90 (1-3), 805–827.
URL http://linkinghub.elsevier.com/retrieve/pii/0045782591901859

de Buhan, P., de Felice, G., 1997. A homogenization approach to the ultimate strength of brick masonry. Journal of the Mechanics and Physics of Solids 45.
URL http://www.sciencedirect.com/science/article/pii/S0022509697000021

de Buhan, P., Dormieux, L., Salençon, J., 1998. Modélisation micropolaire de la résistance d'un milieu renforcé par inclusions. Comptes Rendus de l'Académie des ....
URL http://www.sciencedirect.com/science/article/pii/S1251806999890034

de Buhan, P., Fréard, J., Garnier, D., Maghous, S., Aug. 2002. Failure Properties of Fractured Rock Masses as Anisotropic Homogenized Media. Journal of Engineering Mechanics 128 (8), 869–875.
URL http://ascelibrary.org/doi/pdf/10.1061/(ASCE)0733-9399(2002)128:8(869)http://ascelibrary.org/doi/abs/10.1061/%28ASCE%290733-9399%282002%29128%3A8%28869%29

Eringen, A. C., 1999. Microcontinuum field theories. I: Foundations and solids. Springer, New York.
URL http://www.citeulike.org/group/13900/article/8270507

Florence, C., Sab, K., Jan. 2006. A rigorous homogenization method for the determination of the overall ultimate strength of periodic discrete media and an application to general hexagonal lattices of beams. European Journal of Mechanics - A/Solids 25 (1), 72–97.
URL http://linkinghub.elsevier.com/retrieve/pii/S0997753805000847

Forest, S., Pradel, F., Sab, K., jun 2001. Asymptotic analysis of heterogeneous Cosserat media. International Journal of Solids and Structures 38 (26-27), 4585–4608.
URL http://linkinghub.elsevier.com/retrieve/pii/S002076830000295X

Forest, S., Sab, K., Jul. 1998. Cosserat overall modeling of heterogeneous materials. Mechanics Research Communications 25 (4), 449–454.
URL http://scholar.google.com/scholar?hl=en&btnG=Search&q=intitle:Cosserat+overall+modelling+of+heterogeneous+materials#0http://linkinghub.elsevier.com/retrieve/pii/S0093641398000597

Germain, P., 1973. The method of virtual power in continuum mechanics. Part 2: Microstructure. SIAM Journal on Applied Mathematics 25 (3), 556–575.
URL http://epubs.siam.org/doi/abs/10.1137/0125053

Godio, M., Stefanou, I., Sab, K., Sulem, J., 2015. Dynamic finite element formulation for Cosserat elastic plates. International Journal for Numerical Methods in Engineering 101 (13), 992–1018.
URL http://doi.wiley.com/10.1002/nme.4833

Godio, M., Stefanou, I., Sab, K., Sulem, J., 2016. Multisurface plasticity for Cosserat materials: plate element implementation and validation. International Journal for Numerical Methods in Engineering (108), 456–484.
URL http://doi.wiley.com/10.1002/nme.5219

Itasca Consulting Group, 2013. 3DEC 5.0.

Kim, K. S., 1983. Static and Dynamic Characteristics of Materials with Beam-microstructure. Stanford University.
URL https://books.google.ch/books?id=uZBtNAAACAAJ

Kittel, C., 1996. Introduction to Solid State Physics, 7th Edition. John Wiley & Sons, Inc., New York.

Kumar, R. S., McDowell, D. L., Dec. 2004. Generalized continuum modeling of 2-D periodic cellular solids. International Journal of Solids and Structures 41 (26), 7399–7422.
URL http://linkinghub.elsevier.com/retrieve/pii/S0020768304003658

Lee, J., 1995. Advantages of strain-space formulation in computational plasticity. Computers & structures 54 (3), 515–520.
URL http://www.sciencedirect.com/science/article/pii/0045794994003498

Lippmann, H., 1969. Eine Cosserat-Theorie des plastischen FlieBens. Acta Mechanica 284, 255–284.
URL http://link.springer.com/article/10.1007/BF01182264

Masiani, R., Rizzi, N., Trovalusci, P., Dec. 1995. Masonry as structured continuum. Meccanica 30 (6), 673–683.
URL http://link.springer.com/article/10.1007/BF00986573http://link.springer.com/10.1007/BF00986573

Massart, T., Peerlings, R., Geers, M., Sep. 2004. Mesoscopic modeling of failure and damage-induced anisotropy in brick masonry. European Journal of Mechanics - A/Solids 23 (5), 719–735.
URL http://linkinghub.elsevier.com/retrieve/pii/S0997753804000713

Milani, G., Lourenço, P., Tralli, A., Jan. 2006a. Homogenised limit analysis of masonry walls, Part II: Structural examples. Computers & Structures 84 (3-4), 181–195.
URL http://linkinghub.elsevier.com/retrieve/pii/S0045794905003147

Milani, G., Lourenço, P. B., Tralli, A., Jan. 2006b. Homogenised limit analysis of masonry walls, Part I: Failure surfaces. Computers & Structures 84 (3-4), 166–180.

Milani, G., Taliercio, A., Apr. 2015. In-plane failure surfaces for masonry with joints of finite thickness estimated by a Method of Cells-type approach. Computers & Structures 150, 34–51.
URL http://linkinghub.elsevier.com/retrieve/pii/S0045794914002910

Mindlin, R., 1964. Micro-structure in linear elasticity. Archive for Rational Mechanics and Analysis.
URL http://www.springerlink.com/index/N7078N1674172013.pdf

Mojsilović, N., 2011. Strength of masonry subjected to in-plane loading: A contribution. International Journal of Solids and Structures 48, 865–873.

Mühlhaus, H.-B., 1989. Application of Cosserat theory in numerical solutions of limit load problems. Archive of Applied Mechanics 59, 124–137.
URL http://www.springerlink.com/index/n212407710322312.pdf

Mühlhaus, H.-B., Sulem, J., Unterreiner, P., 1997. Discrete and Continuous Models for Dry Masonry Columns.
URL http://ascelibrary.org/doi/abs/10.1061/(ASCE)0733-9399(1997)123:4(399)

Naghdi, P., Trapp, J., Sep. 1975. The significance of formulating plasticity theory with reference to loading surfaces in strain space. International Journal of Engineering Science 13 (9-10), 785–797.
URL http://linkinghub.elsevier.com/retrieve/pii/0020722575900804http://www.sciencedirect.com/science/article/pii/0020722575900804

Pasternak, E., Mühlhaus, H.-B., jul 2005. Generalised homogenisation procedures for granular materials. Journal of Engineering Mathematics 52 (1), 199–229.
URL http://link.springer.com/10.1007/s10665-004-3950-z

Pau, A., Trovalusci, P., May 2012. Block masonry as equivalent micropolar continua: the role of relative rotations. Acta Mechanica 223 (7), 1455–1471.
URL http://link.springer.com/10.1007/s00707-012-0662-8

Petry, S., Beyer, K., 2014a. Cyclic test data of six unreinforced masonry walls with different boundary conditions. Earthquake Spectra.
URL http://dx.doi.org/10.1193/101513EQS269http://earthquakespectra.org/doi/abs/10.1193/101513EQS269

Petry, S., Beyer, K., 2014b. Influence of boundary conditions and size effect on the drift capacity of URM walls. Engineering Structures 65, 76–88.
URL http://dx.doi.org/10.1016/j.engstruct.2014.01.048

Pietruszczak, S., Ushaksaraei, R., Jul. 2003. Description of inelastic behaviour of structural masonry. International Journal of Solids and Structures 40 (15), 4003–4019.
URL http://linkinghub.elsevier.com/retrieve/pii/S0020768303001744

Pradel, F., Sab, K., 1998. Cosserat modelling of elastic periodic lattice structures. Comptes Rendus de l'Académie des Sciences-Series . . . , 699–704.
URL http://www.sciencedirect.com/science/article/pii/S125180699880002X

Rezakhani, R., Cusatis, G., 2016. Asymptotic expansion homogenization of discrete fine-scale models with rotational degrees of freedom for the simulation of quasi-brittle materials. Journal of the Mechanics and Physics of Solids.

Sab, K., Sep. 2003. Yield design of thin periodic plates by a homogenization technique and an application to masonry walls. Comptes Rendus Mécanique 331 (9), 641–646.
URL http://linkinghub.elsevier.com/retrieve/pii/S163107210300144X

Sab, K., Cecchi, A., Dallot, J., 2007. Determination of the overall yield strength domain of out-of-plane loaded brick masonry. International Journal for Multiscale Computational Engineering, 1–20.

URL http://www.dl.begellhouse.com/journals/61fd1b191cf7e96f,25cc62a120ff4480,7e369b2422df452a.html
Salençon, J., May 2013. Yield Design. John Wiley & Sons, Inc., Hoboken, NJ USA.
URL http://doi.wiley.com/10.1002/9781118648988
Salerno, G., de Felice, G., Mar. 2009. Continuum modeling of periodic brickwork. International Journal of Solids and Structures 46 (5), 1251–1267.
URL http://linkinghub.elsevier.com/retrieve/pii/S0020768308004642
Schaefer, H., 1967. Analysis der Motorfelder im Cosserat-Kontinuum. ZAMM - Journal of Applied Mathematics and Mechanics / Zeitschrift für Angewandte Mathematik und Mechanik 47, 319–328.
URL http://www.neo-classical-physics.info/uploads/3/0/6/5/3065888/schaefer_-_motor_fields_in_cosserat_continua.pdf
Simo, J., Hughes, T., 1998. Computational inelasticity.
URL http://www.ulb.tu-darmstadt.de/tocs/127987207.pdf
Stefanou, I., Sab, K., Heck, J.-V., 2015. Three dimensional homogenization of masonry structures with building blocks of finite strength: A closed form strength domain. International Journal of Solids and Structures 54, 258–270.
URL http://dx.doi.org/10.1016/j.ijsolstr.2014.10.007
Stefanou, I., Sulem, J., 2012. Micromorphic Continua: Application To the Homogenization of Diatomic Masonry Columns. International Journal for Multiscale Computational Engineering 10 (6), 599–613.
URL http://www.dl.begellhouse.com/journals/61fd1b191cf7e96f,3089bea11cd334bd,506f8a524b9d39d0.html
Stefanou, I., Sulem, J., Vardoulakis, I., Feb. 2008. Three-dimensional Cosserat homogenization of masonry structures: Elasticity. Acta Geotechnica 3 (1), 71–83.
URL http://link.springer.com/10.1007/s11440-007-0051-y
Stefanou, I., Sulem, J., Vardoulakis, I., Jun. 2010. Homogenization of interlocking masonry structures using a generalized differential expansion technique. International Journal of Solids and Structures 47 (11-12), 1522–1536.
URL http://linkinghub.elsevier.com/retrieve/pii/S0020768310000533
Steinmann, P., 1994. Theory of finite deformation and finite rotation multiplicative elastoplasticity. International Journal of Solids and Structures 31 (8), 1063–1084.
Sulem, J., Mühlhaus, H.-B., Jan. 1997. A continuum model for periodic two-dimensional block structures. Mechanics of Cohesive-frictional Materials 2 (1), 31–46.
URL http://onlinelibrary.wiley.com/doi/10.1002/(SICI)1099-1484(199701)2:1<31::AID-CFM24>3.0.CO;2-O/abstracthttp://doi.wiley.com/10.1002/%28SICI%291099-1484%28199701%292%3A1%3C31%3A%3AAID-CFM24%3E3.0.CO%3B2-O
Sulem, J., Stefanou, I., 2016. Thermal and chemical effects in shear and compaction bands. Geomechanics for Energy and the Environment 6, 4–21.
URL http://dx.doi.org/10.1016/j.gete.2015.12.004
Sulem, J., Stefanou, I., Veveakis, E., Feb. 2011. Stability analysis of undrained adiabatic shearing of a rock layer with Cosserat microstructure. Granular Matter 13 (3), 261–268.
URL http://link.springer.com/10.1007/s10035-010-0244-1
Suquet, P., 1983. Limit Analysis and Homogenisation. Comptes Rendus Mécanique 296 (5), 1355–1358.
Trovalusci, P., Masiani, R., Mar. 2003. Non-linear micropolar and classical continua for anisotropic discontinuous materials. International Journal of Solids and Structures 40 (5), 1281–1297.
URL http://linkinghub.elsevier.com/retrieve/pii/S002076830200584X
Trovalusci, P., Masiani, R., Oct. 2005. A multifield model for blocky materials based on multiscale description. International Journal of Solids and Structures 42 (21-22), 5778–5794.
URL http://linkinghub.elsevier.com/retrieve/pii/S0020768305001381
Trovalusci, P., Pau, A., Aug. 2014. Derivation of microstructured continua from lattice systems via principle of virtual works: the case of masonry-like materials as micropolar, second gradient and classical continua. Acta Mechanica 225 (1), 157–177.
URL http://link.springer.com/10.1007/s00707-013-0936-9
Vardoulakis, I., Sulem, J., 1995. Bifurcation analysis in geomechanics. Blackie Academic and Professional, Glasgow.
URL http://books.google.com/books?hl=en&lr=&id=W8K79FaiQTwC&oi=fnd&pg=PP1&dq=Bifurcation+analysis+in+geomechanics&ots=nyVBR5mlFs&sig=2QjiIdEIUW9IgobkygrQ4qxHv8U